

**THREE-DEGREES-OF-FREEDOM MEMS
ELECTROSTATIC OUT-OF-PLANE COMB-DRIVE
ACTUATOR FOR AUTO-FOCUS AND IMAGE
STABILIZATION IN PHONE CAMERAS**

by

Faez Saleh Ahmed Ba Tis

A thesis submitted in conformity with the requirements
for the degree of Masters of Applied Science
Mechanical and Industrial Engineering Department
University of Toronto

THREE-DEGREES-OF-FREEDOM MEMS ELECTROSTATIC OUT-OF-PLANE COMB-DRIVE ACTUATOR FOR AUTO- FOCUS AND IMAGE STABILIZATION IN PHONE CAMERAS

Faez Saleh Ahmed Ba Tis

Masters of Applied Science

Mechanical and Industrial Engineering Department
University of Toronto

2014

Abstract

Two versions of a novel three-degrees-of-freedom MEMS electrostatic vertical comb-drive actuator were developed, fabricated, and demonstrated. The novel actuator utilizes a flexure mechanism in which the in-plane (x - y) stiffness is high compared to the out-of-plane (z -axis) stiffness, allowing the actuator to achieve large stroke along the z -axis. The first actuator was able to achieve a large pure translation of 28 μm at 80 V without a stroke magnification mechanism, and also achieve an angle of rotation of 0.78° at 70 V. The second actuator was able to vertically displace a 3 mg mass for 13.5 μm at 80 V. Two enhanced designs of the 3-DOF actuator were also proposed and modelled and analyzed using CoventorWare. These actuators are developed specifically for Auto-Focus (AF) and Optical Image Stabilization (OIS) in phone cameras. Both designs meet the requirements of AF and OIS in phone cameras based on the numerical simulations results.

Acknowledgments

I would like to express my sincere gratitude to my supervisor Ridha Ben Mrad for his continuous support, help and motivation all along the way of achieving my master degree. I would also like thank him of being a minded person to ideas, and encouraging me to shape my research interests.

I would also like to thank Peng Yang and CMC Microsystems for their support for fabricating the actuators in the trial run of the MASP process, and for the financial assistance provided by CMC.

My thanks are also extended to my fellow labmates at the Mechatronics and Microsystems Design Laboratory (MMDL) James Chong, Alaeddin Bani Milhin, Khalil Zahar, Vainatey Kulkarni, Ali Madani, Steffen Blume, and Donn Pasiliao for their technical support when it is needed.

I would also like to express my gratitude to my beloved parents and family for their kindness and support throughout my master program.

Table of Contents

Acknowledgments	iii
Table of Contents	iv
List of Tables	vii
List of Figures.....	viii
Chapter 1 Introduction	1
1.1 Motivation.....	1
1.2 Literature Review.....	2
1.2.1 Image Stabilization in Phone Cameras	2
1.2.2 Auto-focus in Phone Cameras	4
1.3 Structure of the Thesis	12
1.4 Objectives of the Thesis.....	13
Chapter 2 Conceptual Design	15
2.1. Introduction.....	15
2.2. Lateral Instability Analysis	15
2.2.1. Lateral Instability in an In-plane Comb-drive Actuator	16
2.2.2. Lateral Instability in Pure Translation VCDA.....	17
2.3. Description of a Novel Flexure Mechanism	21
2.4. Validation of the Concept	23
2.5. A 3-DOF MEMS electrostatic VCDA.....	25
2.5.1. The Structure of the Actuator	25
2.5.2. Principle of Operation.....	27

2.5.3. Finite Element Analysis (FEA).....	28
2.6. Version 2 of the 3-DOF MEMS Electrostatic VCDA	33
Finite Element Analysis (FEA).....	35
Chapter 3 Applications of the Novel 3-DOF MEMS Electrostatic VCDA	38
3.1. AF Actuator	39
3.1.1. Structure of the Actuator.....	39
3.1.2. Principle of Operation.....	41
3.1.3. Finite Element Analysis (FEA).....	42
3.2. OIS Actuator	44
3.2.1. Structure of the Actuator.....	44
3.2.2. Principle of Operation.....	46
3.2.3. Finite Element Analysis (FEA).....	46
Chapter 4 Fabrication Process	49
4.1. Fabrication Process of VCDA 1and VCDA 2	49
4.2. Fabrication Process of AF and OIS Actuators	52
4.3. Modified Recipe of MASP Fabrication Process	53
4.3.1. Base SOI Wafer Fabrication (Lower Structure)	54
4.3.2. Mirror SOI Wafer Fabrication (Upper Structure)	58
Chapter 5 Experimental Analysis	63
5.1. Static and Dynamic Analysis of VCDA 1.....	63
5.1.1. Translation Mode Analysis	63
5.1.2. Rotation Mode Analysis	66

5.2. Output Force Analysis	68
5.2.1. Static Performance of the VCDA 2	69
5.2.2. Dynamic Performance of VCDA 2.....	70
Chapter 6 Conclusions and Contributions.....	72
6.1. Conclusions.....	72
6.2. Contributions.....	73
6.3. Recommendations.....	73
References	75
Appendix A	79
Appendix B	80
Appendix C	81
Appendix D	82

List of Tables

Table 1-1. Characteristics of AF technologies in phone cameras.....	9
Table 2-1. Specifications of VCDA 1.....	27
Table 2-2. Specifications of VCDA 2.....	34
Table 3-1. Specifications of the novel AF actuator	41
Table 3-2. Specifications of the novel OIS actuator	46
Table 5-1. Comparison between the MASP and the modified MASP fabrication processes.....	53

List of Figures

Figure 1-1. Structure of a conventional VCM for AF in phone cameras [3].....	5
Figure 1-2: schematic of a cross-sectional view of Polight polymer lens. (a) before actuation. (b) during the actuation [23].....	6
Figure 1-3. Illustration of an in-plane comb-drive actuator.....	8
Figure 1-4. Basic design of a parallel plate actuator.....	10
Figure 1-5. Illustration of an out-of-plane comb-drive actuator	11
Figure 2-1. Top view of an in-plane electrostatic comb-drive actuator. (a) Before actuation. (b) Forces generated during actuation.	17
Figure 2-2. Schematic of a conventional vertical comb-drive actuator.....	17
Figure 2-3. Schematic of a conventional vertical comb-drive actuator: top view (up), cross-sectional view (down).	18
Figure 2-4. Schematics of (a) Tow-beam conventional VCDA. (b) Four-beam configuration of the novel VCDA.	21
Figure 2-5. Schematics of (a) Four-beam VCDA. (b) Four-beam VCDA with circular fingers. (c) Three-beam VCDA with circular fingers.	22
Figure 2-6. First mode for both configurations of the VCDA. (a) two-beam configuration. (b) four-beam configuration.	23
Figure 2-7. Maximum pure translation stroke achieved by both configurations. (a) two-beam VCDA. (b) four-beam VCDA.....	24
Figure 2-8. Schematics of the stators (lower structure) of the VCDA 1.....	25

Figure 2-9. Schematics of the rotor (upper structure) of the actuator: top view (left), and isometric view (right).....	26
Figure 2-10. Schematic of the 3D model of the 3-DOF MEMS actuator after bonding – VCDA 1.	26
Figure 2-11. CoventorWare 3D model of the VCDA 1	28
Figure 2-12. Maximum vertical translation stroke of VCDA 1 at 70 V.....	29
Figure 2-13. Displacement versus voltage of VCDA 1.....	29
Figure 2-14. First three modes of VCDA 1. (a) First mode: 959 Hz. (b) Second mode: 2553 Hz. (3) Third mode: 2560 Hz.	30
Figure 2-15. The dynamic performance of VCDA 1 in the frequency domain. (a) Magnitude response. (b) Phase response.....	31
Figure 2-16. Maximum angular stroke of the simulated model of VCDA 1 at 70 V.	32
Figure 2-17. Angle versus applied voltage for VCDA 1 in the rotation mode.....	32
Figure 2-18. Schematics of VCDA 2. (a) Rotors. (b) Stators. (c) Final structure of the actuator with both rotor and stators.	34
Figure 2-19. Simulation of the first mode of VCDA 2.	35
Figure 2-20. Maximum vertical stroke of simulated model of VCDA 2 at 50 V.....	36
Figure 2-21. Translation stroke of the outer rotor of VCDA 2.....	36
Figure 2-22. Simulations of the dynamic performance of outer rotor of VCDA 2 in the frequency domain. (a) Magnitude response. (b) Phase response.....	37
Figure 3-1. Schematics of the stator (lower structure) of the AF actuator: top view (left) and isometric view (right).....	40
Figure 3-2. Schematics of the rotor (upper structure) of the AF actuator.....	40

Figure 3-3. Schematic of 3D model of the AF actuator after bonding.....	41
Figure 3-4. Maximum translation stroke of the AF actuator holding a mass of 3 mg at 70 V....	42
Figure 3-5. Displacement versus voltage for the AF actuator.....	43
Figure 3-6. Dynamic performance of the AF actuator in the frequency domain. (a) Magnitude response. (b) Phase response.....	43
Figure 3-7. Schematics of the rotor (upper structure) of the OIS actuator: top view (left) and isometric view (right).....	44
Figure 3-8. Schematics of the stators (lower structure) of the OIS actuator: top view (left) and isometric view (right).....	45
Figure 3-9. Schematic of the OIS actuator after bonding.....	45
Figure 3-10. Displacement versus voltage of the OIS actuator.....	47
Figure 3-11. Maximum angular stroke of the simulated model of the OIS actuator holding a mass of 560 mg at 140 V.	47
Figure 3-12. Dynamic performance of the OIS actuator in the frequency domain. (a) Magnitude response. (b) Phase response.....	48
Figure 4-1. The MASP fabrication process. (a) Fabrication of a Base SOI wafer. (b) Fabrication of mirror device layer. (c) Bonding of both SOI wafers. (d) Final structure of the actuator.....	50
Figure 4-2. SEM micrographs of the VCDA 1 (right) and VCDA 2 (Left) prototypes.	50
Figure 4-3. SEM micrograph of the gap between adjacent electrodes of the actuator.....	51
Figure 4-4. Packaged chip of VCDA 1.....	51
Figure 5-1. Setup used for the static and dynamic performance testing of the actuator in the translation mode.....	63
Figure 5-2. Displacement versus voltage of VCDA 1 in the translation mode.	64

Figure 5-3. Dynamic performance of VCDA 1 in the time domain. (a) Step input of 0 to 40V. (b) Step input of 40 V to 0 V	65
Figure 5-4. Dynamic performance of the translation stroke of VCDA 1 in the frequency domain. (a) Magnitude response. (b) Phase response.....	66
Figure 5-5. Setup used for the static and dynamic performance testing of the actuator in the rotation mode.	67
Figure 5-6. Angle of rotation versus applied voltage of VCDA 1 in the rotation mode.	67
Figure 5-7. Time domain response of VCDA 1 in the rotation mode. (a) Step of 0 to 40V. (b) Step input of 40 V to 0 V	68
Figure 5-8. Snapshot of VCDA 2 loaded with a mass of 3 mg during the testing.	69
Figure 5-9. Static performance of the translational stroke of the outer rotor of VCDA 2 in the unloaded and loaded states.....	70
Figure 5-10. Dynamic performance of the unloaded outer rotor of VCDA 2 in the time domain. (a) Step input of 0 to 80 V. (b) Step input of 80 V to 0 V.	71
Figure 5-11. Dynamic performance of the 3 mg loaded outer rotor of VCDA 2 in the time domain. (a) Step input of 0 to 80V. (b) Step input of 80 V to 0 V.	71
Figure A-1. GDS mask layers forVCDA 1.....	79
Figure B-1. GDS mask layers for VCDA 2.	80
Figure C-1. GDS mask layers for AF actuator.	81
Figure D-1. GDS mask layers for OIS Actuator.....	82

Chapter 1

Introduction

1.1 Motivation

As cell phone technology and capabilities advance, the need for high performance miniature cameras is becoming more urgent. There are almost two billion miniature cameras that are manufactured annually of which 40% offer the Auto-Focus (AF) feature. In cameras that offer AF, an actuation method is used to move or modify the shape of one or more lenses to achieve an improved sharpness of the image. As the distance to an object changes, its image gets blurred, and thus in order to bring the image into focus, the focal length of the lens is adjusted [1][2].

Many actuation methods have been used to achieve auto-focusing in phone cameras. These include Voice Coil Motors (VCM), piezoelectric actuators, MEMS electrostatic actuators, and liquid lens actuators [3][4][5]. VCM is the most commonly used actuator in commercial phone cameras. VCM works on the principle of electromagnetic actuation; however, it is known to have a number of disadvantages such as a high power consumption, slow response speed and large size [1][2]. Piezoelectric actuation is also used to achieve autofocus; nevertheless, it exhibits motion control degradation which leads to the need for position sensor; and also the sensitivity of the piezoelectric material to temperature [2][6][7]. Liquid lens technology is under development, and is known to require high power, offers a slow response speed and sets stringent demands on packaging [7].

In today's competitive smart phone market, cell phones need to be thin. Consequently, the camera module integrated within the phones also needs to be thin. The following are now required features of an actuator for AF in phone cameras [1]:

- 1- Small size : < (9x9x1) mm
- 2- Low power consumption: < 5 mW
- 3- Fast response speed: < 10 ms

Based on the above requirements, MEMS electrostatic actuation is a technology that can be used to achieve the AF in cell phone cameras. MEMS electrostatic actuation is known to offer very low power consumption and a fast response speed where the transition speed in electrostatic

actuators is governed largely by the charge and discharge time of the capacitor. Only one MEMS electrostatic actuator, developed recently by Digital Optics Corporation (DOC), is used to achieve auto-focus in phone cameras; however, this actuator requires a complex fabrication process; and leads to an undesirable lens tilt that compromises the image quality [1][8].

Another desirable and important feature of phone cameras is optical image stabilization which is used to eliminate undesired effects of hand shaking on the images. Currently, only two models of commercial cell phones have Optical Image Stabilization (OIS) features. These are the Nokia Lumia (920, 1020) and the HTC One. Both OIS systems use electromagnetic actuation.

This thesis thus presents a novel MEMS electrostatic actuator platform that:

- Achieves AF while offering low power consumption, high response speed, and no lens tilt;
- Achieves OIS while offering low power consumption, and high response speed;
- Can be fabricated using standard fabrication process.

1.2 Literature Review

1.2.1 Image Stabilization in Phone Cameras

Hand motion is considered the main sources of image blur in cell phone and digital still cameras. Hand motion has three rotation components: yaw, pitch and roll. Several studies have investigated and characterized hand motion, and have indicated that the frequency of the hand motion is in the interval of 8 to 12 Hz and that the angle of yaw and pitch rotations is approximately 0.6° [9][10][11]. There are two main types of image stabilization techniques: optical and digital image stabilizations.

Optical Image Stabilization (OIS) utilizes a mechanical actuation method to move, or modify, one or more optical elements to eliminate the effect of the hand motion on the image quality. It includes three main techniques: lens-based OIS, sensor-shift OIS, and camera module rotation OIS. The first two techniques are typically realized using electromagnetic or piezoelectric actuators to move either the lens barrel or the image sensor vertically in the x - y plane to compensate for the hand motion. In the camera module rotation OIS, the whole module (lens

barrel and image sensor) is rotated to cancel the effect of yaw and pitch rotations of the hand. This latter technique is known to produce the best image quality compared to the first two techniques [11][12][13].

The other type of image stabilization is the digital (electronic) image stabilization which does not include movements of the optical elements; rather it uses software algorithms to process the image after it has been captured by the sensor. However, this type of image stabilization is not as effective in eliminating hand shaking blur as OIS[11].

In commercial phone cameras, OIS has been only used in Nokia Lumia (920, 1020) and HTC-One phones [14][15]. In the OIS of Nokia Lumia mobile phones, the lens barrel is rotated using an electromagnetic actuator to compensate for the yaw and pitch rotations of the hand. Additionally, a variable prism is sandwiched between the image sensor and the lens holder in order to maintain the focal plane on the image sensor plane independently from the image stabilization. Two gyroscopic sensors are mounted to the camera module to measure the amount of hand rotations and send the signal to the lens actuator in order to rotate conversely to cancel the hand motion effect. This technology works using electromagnetic actuation which leads to high power consumption [14].

Other three OIS technologies that can be used in mobile phones, but are still under evaluation, are the liquid lens-based; MEMS-based; and Shape Memory Alloy (SMA)-based optical image stabilizations. The first technology was developed by VariOptics Inc., which can be realized by applying voltage to a lens that contains two transparent liquids, creating an electric field that results in a change of the refractive indices of the liquids. This change can be utilized to compensate for any undesired hand motion. This technology operates at a high response speed; however, it causes a vignetting effect at the edges of the image because the focal plane does not coincide with the image sensor plane [16].

The second technology, the MEMS-based OIS, was developed by Digital Optics Corporation (DOC), and it consists of three main in-plane comb-drive actuators that are connected to the edges of a lens. When the comb-drives are actuated, each comb applies a tangential force to the lens and consequently moves the lens on an in-plane motion. Although this technology offers a high response speed and requires low power, it is controlled by complicated algorithms because the motion involves rotation about the optical axis (z -axis) and translation in the x - y plane[17].

The third technology, the SMA-based OIS, was developed by Cambridge Mechatronics Limited. It works using the camera module rotation OIS technique based on four shape memory wires surrounding the camera module. When a voltage is applied to one wire, it heats and shrinks causing the corresponding side of the module to move down vertically, thus the camera module rotates. Although this technology utilizes the best technique to achieve OIS, i.e. module rotation OIS, it has a slow response speed and a high power consumption. In addition, the sensitivity of the SMA to temperature changes complicates the control when OIS is attempted [12].

1.2.2 Auto-focus in Phone Cameras

Different types of actuators have been used to achieve AF in phone cameras. In general, there are two main mechanisms to achieve AF: lens-motion and lens-modification. In the former, one or more lenses move back and forth to achieve a sharp image. In case of moving only single lens of inside lens barrel, the required traveling stroke is 80 μm , whereas in the case of moving the entire lens barrel, the required traveling stroke is 250 μm [1][7]. The lens-motion type includes Voice Coil Motors (VCM), piezoelectric actuators, and MEMS electrostatic actuators; whereas in the latter, the lens itself changes its focal length by using liquids or piezoelectric actuation to achieve the AF [3][4][7].

1.2.2.1 Electromagnetic Actuation

Electromagnetic actuators operate based on the electromagnetic force equation

$$\vec{F}_{\text{mag}} = q\vec{v} \times \vec{B} \quad (1-1)$$

where F_{mag} is the magnetic force acting on a particle of electric charge q with instantaneous velocity v , and B is the magnetic field. When a current-carrying conductor is placed in a static magnetic field, the instantaneous magnetic field around the conductor interacts with the static magnetic field and produces a force. The applied force depends on both the field from the coils and the magnet [18]. Voice Coil Motors (VCM), used in autofocus cameras, work on this principle. These VCMs mainly consist of two parts: moving and fixed. The former, consists of a lens module, a lens holder, and a coil; and the latter consists of two permanent magnets, a yoke, and a base, as depicted in Figure 1-1[3]. As the current passes through the coil, a magnetic field

develops around it, and this magnetic field pushes away the permanent magnets; resulting in a vertical movement of the lens barrel.

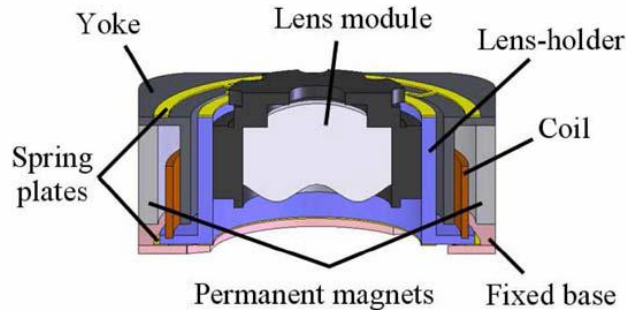


Figure 1-1. Structure of a conventional VCM for AF in phone cameras [3].

The VCM is widely used to achieve the AF in digital still cameras; however, when it is used in miniature cameras it compromises the image quality. The drawbacks of VCM include high power consumption, slow response speed, large size, and undesired lens tilt of 0.2° which results in a deterioration of the image quality [1][7][3].

1.2.2.2 Piezoelectric Actuation

Piezoelectricity can be defined as the electric charge that accumulates in some solid materials, such as crystals and certain ceramics, when they are subjected to mechanical stress. This is known as the direct effect of piezoelectricity. Alternatively, if an electric field is applied, the same material would deform. This is referred to as the inverse effect of piezoelectricity [19][20]. The microscopic origin of piezoelectricity is the displacement of ionic charges inside the crystals, which causes the polarization and hence an electric field is generated. When a mechanical stress is applied, the space between the centers of positive and negative charge positions would change in each domain cell. Conversely, when an external electric field is applied, a force would be generated between the centers of positive and negative charges, resulting in an elastic strain of the piezoelectric material [21][22].

For the auto-focus in phone cameras application, New Scale Technology Inc. developed a piezoelectric motor, called UTAF. It consists of a threaded screw and a mating nut which ultrasonically vibrates and causes the screw to turn, generating a linear motion. The actuator

provides a large stroke at high speed; however, it needs a sensor for positioning, it is large in size and is sensitive to temperature [7][6].

Another lens-modification-based piezoelectric actuator, used for auto-focusing, was developed by Polight Technologies. It operates based on the unique design of a polymer lens (called Tlens); in which a ring piezoelectric thin film, acts as an actuator, is embedded into a deformable thin membrane of glass. The glass, in turn, is deposited on the top of the polymer lens. When a voltage is applied to the ring piezoelectric actuator, radial forces are created, enforcing the glass membrane to bend as shown in Figure 1-2; these curve-like adjustments of the shape of the glass wafer vary the focal length of the polymer lens by changing its refractive index, thus AF is achieved. Although this technology provides high response speed and low power consumption, the polymer lens and piezoelectric material are sensitive to temperature changes [23].

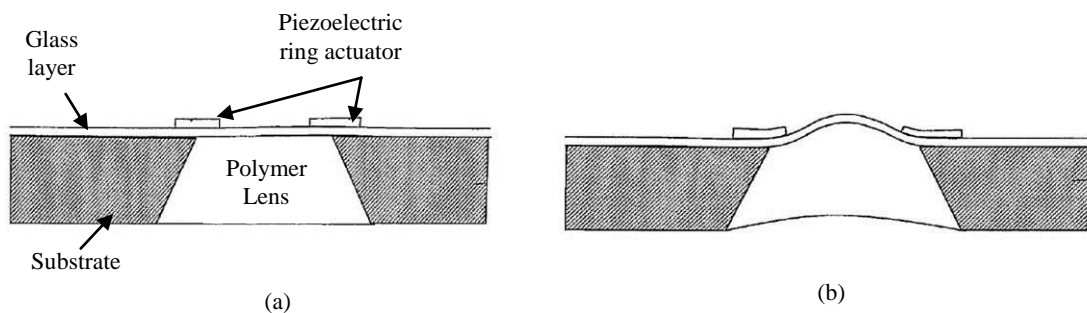


Figure 1-2: schematic of a cross-sectional view of Polight polymer lens. (a) before actuation. (b) during the actuation [23].

1.2.2.3 Liquid Lens Actuation

VariOptics Inc. has developed a liquid lens technology for AF in mobile phone cameras. The technology works on the principle of electrowetting, in which an external voltage is applied across both surfaces (electrodes) of a lens that contains two transparent liquids (water and oil) with different refractive indices. The electric field forces the liquids to be redistributed according to the amount of the applied voltage, changing the lens shape, and resulting in a variation of the focal length of the lens. This technology provides a combination of AF and OIS

features and has been shown to be reliable up to 1 million cycles. However, it has a slow response time of 200 ms, relatively high power consumption and high cost [7][6][24].

1.2.2.4 Electrostatic Actuation

The electrostatic actuation works on the operating principle of the capacitor. When a voltage is applied across two electrodes, an electric field is created between them, and it generates an attractive electrostatic force. In large-scale devices, electrostatic force is not usually used due to the fact that the electrostatic force decreases with the square of the distance between the electrodes. However, in micro-scale devices, electrostatic force is a good candidate for micro actuation because micro devices have large surface-area-to-volume ratios and their masses are small [19]. There are two types of motion produced by electrostatic actuators: in-plane and out-of-plane.

1.2.2.4.1 In-plane Electrostatic Actuators

Lateral comb drive actuators provide in-plane motion. The capacitance of this type of actuators is linear with displacement, resulting in an electrostatic driving force which is independent of the position of the moving fingers [25][26]. The basic design of lateral comb-drive actuator consists of two sets of fingers which are placed in the same plane, opposing each other as shown Figure 1-3. There are two capacitances associated with each finger, one on the left hand side of the finger (C_l) and one on the right hand side (C_r). The values of these capacitances are

$$C_l = C_r = \frac{\epsilon_0 \epsilon_r x_0 h}{g} \quad (1-2)$$

where ϵ_0 is the dielectric constant, ϵ_r is the relative static permittivity, x_0 is the length of the overlapping area, g is the gap between two adjacent fingers, and h is the height of the fingers.

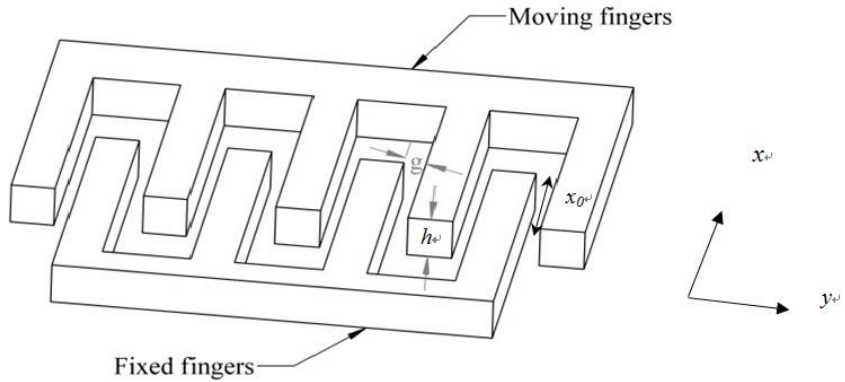


Figure 1-3. Illustration of an in-plane comb-drive actuator.

The electrostatic force of a comb-drive develops between the fingers in the longitudinal direction and can be obtained from an expression of the total stored energy with respect to the axis of motion as follows

$$F_e = \frac{1}{2} \frac{\partial C}{\partial x} V^2 = \frac{1}{2} \frac{N \cdot \epsilon \cdot h}{g} V^2 \quad (1-3)$$

where F_e is the driving electrostatic force, g is the lateral gap between the fingers, h is the height of the fingers, and N is the number of fingers [19].

DOC's MEMS AF actuator [8] works on the electrostatic actuation principle. It consists of a number of in-plane comb-drive actuators which are connected to a single lens using supporting beams. The initial motion of the comb-drives is an in-plane motion which is, then, converted into an out-of-plane motion to move the lens in the vertical direction. This technology utilizes the translation of a single lens for a stroke of $80 \mu\text{m}$ instead of moving the lens barrel for $200 \mu\text{m}$ as is done by the VCM based technology. Despite the fact that this technology does not have the drawbacks associated with the VCM and piezoelectric actuators, it leads to an undesirable lens tilt of 0.05° and it requires complex fabrication steps to achieve the conversion of the in-plane to the out-of-plane motion [1][8].

The following table summarizes the features of the current AF technologies [6].

Features	DOC MEMS actuator	VCM	Polight piezoelectric Actuator	New Scale piezoelectric Actuator	Liquid Lens
Actuator size (mm)	7x7x0.15	8.5x8.5x5	4.2 x 4.2 x 0.5	8.5x8.5x5	7.75(circle diameter)x2
Module size (mm)	8.5x8.5x6	10x10x8.5	-	8.5x8.5x6	8.5x8.5x7
Imager resolution (MP)	8	8	8	8	3
Peak power (mW)	0.5	250	1	80	8
Repeatability (μm)	1	10	-	Need position sensor	-
Speed (ms)	10	30	1	30	200
Reliability cycles	10 million	100 thousands	-	100 thousands	1 million
Drawbacks	Lens tilt and complex structure	High power, consumption, slow response speed , and large size	Sensitivity of the lens and the piezo materials to temperature	large size, motion control degradation	Low speed, high power consumption

Table 1-1. Characteristics of AF technologies in phone cameras.

It is obvious from the above literature that the electrostatic actuation exhibits numerous advantages over the other technologies in terms of power consumption and response speed. However, the DOC's MEMS AF actuator still has some drawbacks. Therefore, the electrostatic actuation would be further pursued to design a new MEMS electrostatic AF actuator that eliminates the drawbacks of DOC's MEMS AF actuator.

1.2.2.4.2 Out-of-plane Electrostatic Actuators

There are two types of electrostatic actuators that can provide out-of-plane motion, including parallel-plate, and vertical comb-drive actuators. Parallel-plate actuators consist of two conducting plates parallel to each other; one of the plates is moving and the second one is fixed as shown in Figure 1-4. The movable plate is supported by a mechanical spring with constant

(Km). When a voltage is applied across the parallel plates, an electrostatic force is created between them and the magnitude of this force is given by

$$F_e = \frac{\epsilon_0 \epsilon_r A}{2(x_0 + x)^2} V^2 \quad (1-4)$$

where x_0 is the initial gap between the plates, x is the stroke of the moving plate, and A is the area of one plate. The developed electrostatic force between the electrodes moves the free electrode towards the fixed one, resulting in a decrease of the gap between the parallel plates; however, a mechanical force develops in the restoring beams and opposes the electrical force. Consequently, it returns the moving electrode to its equilibrium position when the applied voltage drops [19].

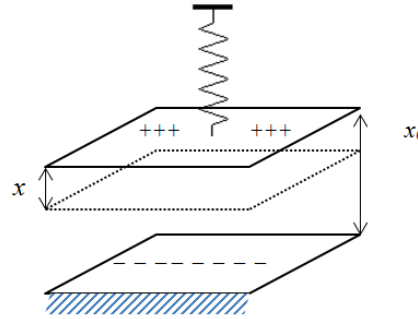


Figure 1-4. Basic design of a parallel plate actuator.

The phenomenon of pull-in effect is usually associated with parallel-plate actuation. In fact, *Pull-in* is the term that describes the snapping of the parallel plates together, limiting the displacement of the moving plate to one third of the initial gap between the plates. This is because of the non-linear relationship between the electrostatic force and the gap distance, as it can be clearly seen in Equation (1-4). At first, the mechanical restoring force increases linearly with displacement of the plate whereas the electrostatic force increases non-linearly, and the pull-in effects takes place when the electrostatic forces exceeds the mechanical restoring force of the springs [27][28][29].

Out-of-plane Comb-drive Actuators

The out-of-plane vertical comb-drive actuator (VCDA) is similar in design to the in-plane comb-drive actuator except that the fingers are vertically arranged with an offset between them as

shown in Figure 1-5. This vertical arrangement enables the fingers to move upward or downward. The out-of-plane motion, in turn, can be either rotational or translational [30][31].

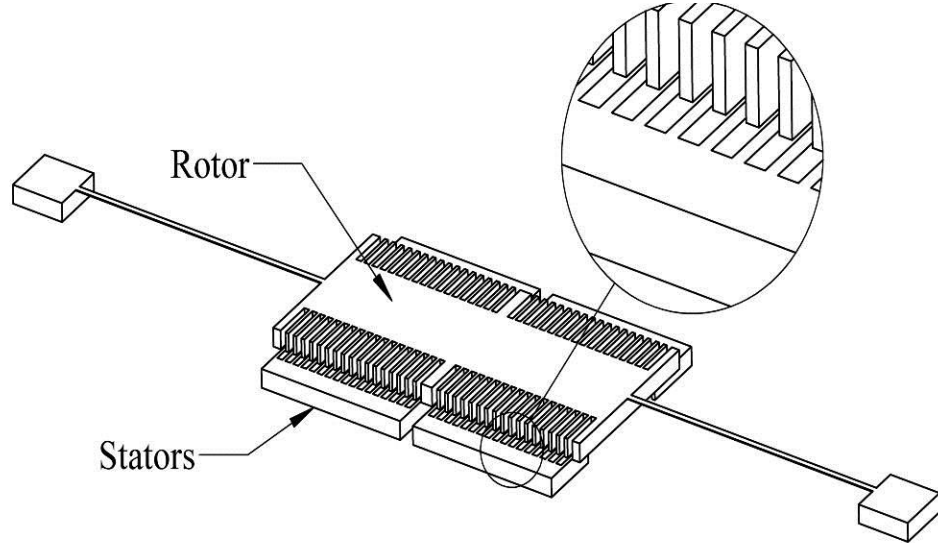


Figure 1-5. Illustration of an out-of-plane comb-drive actuator.

In general, a VCDA produces a rotational motion which can be amplified to produce a larger out-of-plane stroke using a mechanical amplification mechanism. However, during the amplification process, the output force of the actuator significantly decreases.

Different types of large rotational stroke out-of-plane electrostatic actuators have been developed. For example, an electrostatic VCDA, presented in [32], consists of two sets of fingers placed horizontally with a vertical offset between them, and the rotor of the actuator is suspended using two guided cantilever beams, similar to the structure of the VCDA in Figure 1-5. The actuator achieved an angular motion of 18° at a voltage of 150 V.

Another design of an out of-plane electrostatic actuator was developed by He and Ben Mrad [33]. It works on the repulsive force principle, and consists of a two-layer finger structure; the bottom layer consists of two sets of fingers, unaligned fixed and aligned fixed fingers. The latter is aligned with the moving comb fingers in the top layer. All of the fixed fingers are attached to the substrate, and all moving fingers are connected together and supported by suspension springs. The actuator achieved an out-of plane rotational stroke of $86 \mu\text{m}$ at 200 V; however, it provides low output force.

Out-of-plane Pure Translation (piston motion) Electrostatic VCDA

A number of VCDA that provides pure vertical translation in the z -axis were developed. A VCDA was used to actuate a deformable micromirror and achieved a translational stroke of 20 μm at 100 V. It consists of an array of top electrodes (rotor) that are attached to the mirror plate and facing bottom electrodes (stator). The fingers of the rotor and stator interdigitate during the vertical motion [34]. Another VCDA that achieved a piston motion of 15 μm at 140 V was developed by V. Milanovic *et al.* and was fabricated using a MULTILEVEL BEAM SOI-MEMS process. It consists of two sets of fingers placed horizontally with a vertical offset between them. The rotor of the actuator is suspended using two guided cantilever beams and the actuator has a similar structure to that of the VCDA in Figure 1-5. The stroke of this actuator is limited due to a lateral instability that takes place during the movement in the z -axis [32]. Another VCDA that provides a piston motion was developed by E. Carr. Although the actuator is self-aligned, the prototype can only achieve a translational stroke of 1.4 μm due to the high stiffness of the supporting beams in the z -axis [35].

As a summary, the main issues associated with pure translation stroke (piston motion) VCDA are as follows.

- 1- The lateral and angular instabilities of VCDA have limited the angular and the vertical translation stroke. These instabilities are a major problem associated with comb-drive actuators [32][36].
- 2- Most of the VCDA that are fabricated using double-layer fabrication processes suffer from misalignment problems between the adjacent fingers. The misalignment arises when the combs of the actuators are fabricated on separate substrates and, then, bonded. During the bonding step, there is a large likelihood of having a misalignment between the fingers [32][37].

1.3 Structure of the Thesis

In Chapter 2, the conceptual design of the 3-DOF MEMS electrostatic vertical comb-drive actuator is proposed, which includes a description of the novel flexure mechanism of the actuator. Then, two versions (VCDA 1 and VCDA 2) of the novel actuator are presented and

finite element simulation results of the static and dynamic performance characteristics of both versions are presented.

Chapter 3 describes the requirements for the main application of the novel actuator platform: AF and OIS in phone cameras. Simulation results using Finite Element modeling of the static and dynamic performance of the version of the actuators developed for AF and OIS actuators are presented.

In Chapter 4, the fabrication process for the VCDA 1 and VCDA 2 is briefly discussed; followed by a detailed description of a customized fabrication process that was attempted to fabricate the AF and OIS actuators.

In Chapter 5, the static and dynamic experimental analyses of VCDA 1 are presented. The output force analysis of VCDA 2 is also discussed. Conclusions, contributions, and recommendations for future work are summarized in Chapter 6.

1.4 Objectives of the Thesis

The goal of this thesis is to develop a three-degrees-of-freedom MEMS electrostatic vertical comb-drive actuator that provides a large out-of-plane pure translation stroke of up to 80 μm and a rotation of 0.6°, responds at high speed of <10 ms, and consumes minimal power. The actuator will be used in auto-focus and image stabilization applications to displace a lens of 3 mg in mass for autofocusing, and rotates the complete camera module of 560 mg for optical image stabilization. The detailed list of the objectives is as follows:

- To design and develop a novel three-degrees-of-freedom MEMS electrostatic vertical comb-drive actuator platform that translates in z -axis and rotates about the x and y axes
- To fabricate and experimentally characterize the novel actuator
- To develop a customized version of the three-degrees-of-freedom MEMS electrostatic vertical comb-drive actuator to be used for AF that is able to move a lens of 3 mg in mass up to 80 μm while operating at high speed (a response speed of < 10 ms)

- To develop a customized version of the three-degrees-of-freedom MEMS electrostatic vertical comb-drive actuator to be used for OIS that is able to rotate a camera module of 560 mg in mass up to an angle of 0.6° , while offering a response speed of < 20 ms

Chapter 2

Conceptual Design

2.1. Introduction

In this chapter, a three-degrees-of-freedom MEMS electrostatic vertical comb-drive actuator (VCDA) is presented. The actuator is able to overcome the limitations of the out-of-plane MEMS actuators, such as achieving limited pure translational stroke, providing low output force, and operating at high input voltage. These drawbacks could be attributed to one of the following reasons:

- Lateral and angular instability of the VCDA.
- Misalignment between the fingers of the upper and the lower combs fingers. This is typically due to the fabrication process. In the work presented here, a new fabrication process will be attempted offered by Micralyne (Edmonton, Canada) that claims to address the misalignment issues.

The novel 3-DOF MEMS electrostatic vertical comb-drive actuator eliminates these latter drawbacks of the VCDA by avoiding their sources. It provides a large pure translation stroke, large output force, and operates at a relatively low input voltage. By utilizing a unique flexure mechanism, that has a high stiffness in the x - y plane and low stiffness in the z direction, the actuator is able to achieve a large stroke before exhibiting any lateral instability. Moreover, the accuracy of the Micralyne All-Silicon Platform (MASP) fabrication process has eliminated the misalignment between the comb fingers.

One of the main advantages of the novel actuator platform is its ability to provide a three-degrees-of-freedom motion in comparison to other vertical comb-drive actuators which are limited to one or two degree-of-freedom motion. Based on an extensive study of the literature, no MEMS electrostatic actuator that offers three degrees of freedom motion is available.

2.2. Lateral Instability Analysis

The most significant improvement of the novel three-degrees-of-freedom MEMS electrostatic vertical comb-drive actuator is the flexure mechanism that enables the actuator to overcome the

lateral instability and allow it to achieve a large stroke. Most of the VCDA, fabricated as of now, are suspended by only two beams along one axis, so that they rotate about that axis or move in a pure translation in the z direction. The VCDA that provide rotational motion suffer from an angular instability, whereas the ones that provide pure translation suffer from lateral instability in the x - y plane. Angular instability has been investigated and analyzed extensively [32][36], because the most common use of VCDA is to actuate micromirrors which can be achieved by the angular stroke of VCDA. The lateral instability in the x - y plane has not been widely investigated due to the difficulties in fabricating pure translation VCDA. Therefore, in this section, the lateral instability in the x - y plane of a pure translation VCDA would be discussed in more details in order to develop a deeper insight into the novel flexure mechanism that is part of the current design.

The lateral instability usually occurs when the electrostatic force in the lateral direction of the VCDA is greater than the mechanical restoring force of the supporting beam in that direction. A brief discussion of lateral instability in an in-plane comb-drive actuator would be first presented, followed by an analysis of the lateral instability of a pure translation VCDA.

2.2.1. Lateral Instability in an In-plane Comb-drive Actuator

The instability of the in-plane comb-drive actuator, shown in Figure 2-1, takes place when the electrical spring constant (K_{e_x}) of the electrical force along the x -axis (F_{e_x}) is greater than the mechanical spring constant (Km_x) of the supporting beam. This instability limits the stroke of the actuator; therefore, the maximum stroke along the y -axis (y_c) is governed by the following equation:

$$y_c^2 + y_o \cdot y_o - \frac{Km_x}{Km_y} \frac{g^2}{2} = 0 \quad (2-1)$$

When there is no pre-engagement between the fingers ($y_o = 0$), the previous equation simplifies to

$$y_c^2 = \frac{Km_x}{Km_y} \frac{g^2}{2} \quad (2-2)$$

Therefore, for the actuator to have a large stroke, Km_x has to be very large as compared to Km_y .

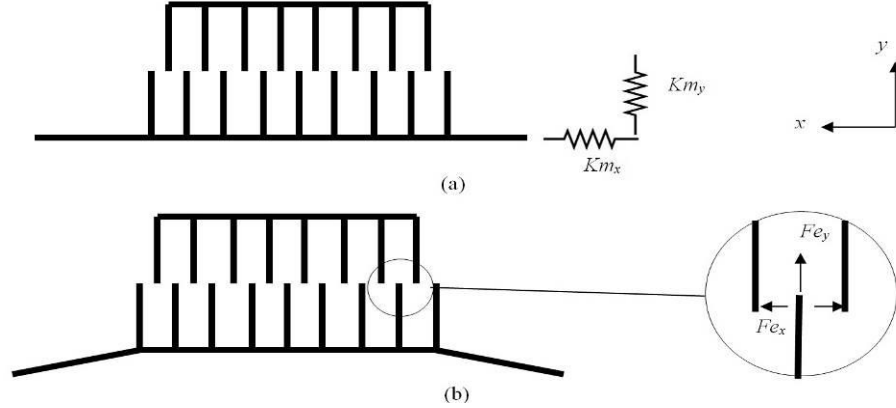


Figure 2-1. Top view of an in-plane electrostatic comb-drive actuator. (a) Before actuation. (b) Forces generated during actuation.

2.2.2. Lateral Instability in Pure Translation VCDA

Similar to the in-plane comb-drive actuator, in order to achieve a large pure translational stroke in the z direction using a VCDA, the resistance to the movement in the x - y plane must be greater than the resistance to movement along the z -axis. In other words, the actuator must be more sensitive in the z direction than the x and y directions (see Figure 2-2). Thus, the spring constants along the x and y axes (Km_x , Km_y) have to be very large compared to the mechanical spring constant along the z axis (Km_z). The lateral instability in the y -axis would occur when the electrical constant (Ke_x) of the electrical force (Fe_x) is greater than the mechanical spring constant along the x -axis, and, similarly, the lateral instability in the y -axis would occur when the electrical constant (Ke_y) of the electrical force (Fe_y) is greater than the mechanical spring constant along the y -axis.

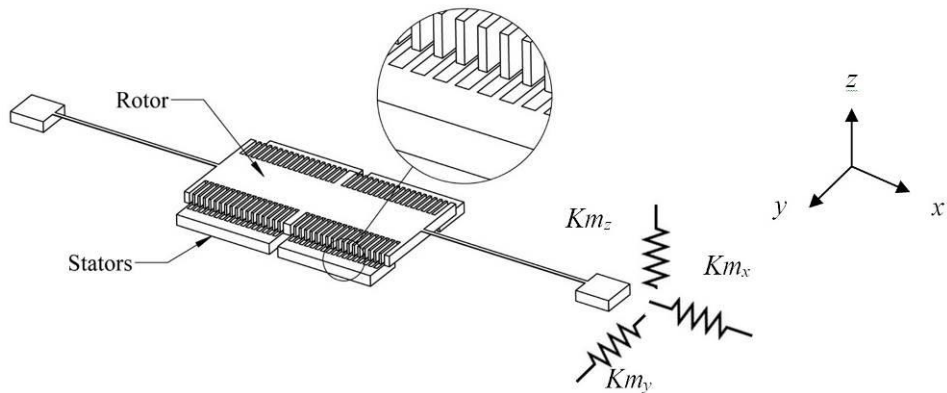


Figure 2-2. Schematic of a conventional vertical comb-drive actuator.

Mathematically, the electrostatic force along the z -axis is calculated by deriving the total energy of the actuator with respect to z (see Figure 2-3). The total energy in the actuator is

$$U_{tot} = \frac{1}{2}V^2C_x + \frac{1}{2}V^2C_y + \frac{1}{2}V^2C_z \quad (2-3)$$

$$U_z = \frac{1}{2}V^2C_z \quad (2-4)$$

$$C_z = \epsilon_0\epsilon_r \frac{y_0 z}{g} \quad (2-5)$$

$$Fe_z = \frac{\partial U_z}{\partial C} = \frac{1}{2}\epsilon_0\epsilon_r \frac{y_0}{g} V^2 \quad (2-6)$$

Fe_z is the electrostatic force that moves a free comb finger to a fixed one along the z direction. But the forces in the x and y directions are the ones that causes the lateral instability.

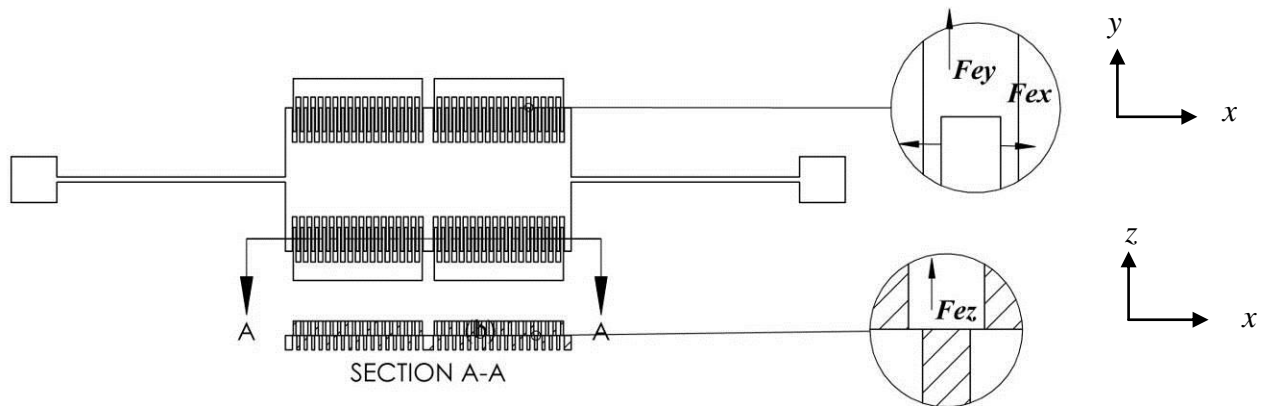


Figure 2-3. Schematic of a conventional vertical comb-drive actuator: top view (up), cross-sectional view (down).

To find Fe_x and Fe_y , the energy equation is differentiated.

$$U_x = \frac{1}{2}V^2C_x \quad (2-7)$$

$$C_x = \epsilon_0 \epsilon_r \frac{yz_0}{g_x} \quad (2-8)$$

$$Fe_x = \frac{\partial U_x}{\partial x} = \frac{1}{2} \epsilon_0 \epsilon_r yz V^2 \left(\frac{1}{(g-x)^2} - \frac{1}{(g+x)^2} \right) \quad (2-9)$$

And the effective negative electrostatic spring constant at $x = 0$ is obtained by deriving the Fe_x along x -axis

$$Ke_x = \frac{\partial Fe_x}{\partial x} \left| \frac{1}{2} \epsilon_0 \epsilon_r yz V^2 \left(\frac{2}{(g-x)^3} - \frac{-2}{(g+x)^3} \right) \right|_{x=0} \quad (2-10)$$

$$Ke_x = \frac{2 \epsilon_0 \epsilon_r yz V^2}{g^3} \quad (2-11)$$

Similarly for the y -axis,

$$U_y = \frac{1}{2} C_y V^2 \quad (2-12)$$

$$C_y = \epsilon_0 \epsilon_r \frac{yz}{g} \quad (2-13)$$

$$Fe_y = \frac{\partial U_x}{\partial C} = 2 \left(\frac{1}{2} \epsilon_0 \epsilon_r \frac{z}{g} V^2 \right) \quad (2-14)$$

The condition needed to prevent the instability along the x -axis is

$$Km_x > Ke_x \quad (2-15)$$

By substituting the value of Ke_x from Equation (2-11) into Equation (2-15), the following is obtained:

$$Km_x > \frac{2\epsilon_0\epsilon_r y z V^2}{g^3} \quad (2-16)$$

To find the stroke along the z -axis, the electrostatic force along the z -axis is set equal to the mechanical restoring force along the same axis

$$Fe_z = Fm_z \quad (2-17)$$

$$Km_z Z = 2 \left(\frac{1}{2} \epsilon_0 \epsilon_r \frac{y}{g} V^2 \right) \quad (2-18)$$

By solving Equation (2-16) for V^2 to obtain the critical value for the voltage that leads to lateral instability and substituting it in Equation (2-18), the critical displacement along the z -axis would be:

$$Z_c^2 = \frac{Km_x}{Km_z} \frac{g^2}{2} \quad (2-19)$$

Based on Equation (2-19), in order to have a larger displacement along the z -axis without instability in the x -direction, a higher Km_x compared to Km_z is required.

The same analysis is applied along the y -axis. The mechanical force stored in the supporting beam is set equal to the electrostatic force in that direction.

$$Fm_y = Fe_y \quad (2-20)$$

$$Km_y \cdot Y = 2 \left(\frac{1}{2} \epsilon_0 \epsilon_r \frac{z}{g} V^2 \right) \quad (2-21)$$

To have a large stroke in the z -axis, the displacement in the y -axis must also be maintained low. Therefore, the supporting beams have to be stiff along the y -axis in order to overcome the electrical force in the y -axis during translation along the z -axis.

As a summary, in order to design a large stroke vertical comb-drive actuator, high stiffness of the supporting beams along the y and x axes compared to the stiffness along the z -axis is required.

2.3. Description of a Novel Flexure Mechanism

The conventional vertical comb drive actuator is supported by two guided cantilever beams along one axis; see Figure 2-2(a). In a two-beam configuration of a VCDA, the free moving comb would experience the maximum resistance to movement in the x -axis, as it would be resisted by the longitudinal direction of the beams. The second highest resistance to movement would be along the y -axis as it would be resisted by the lateral bending stress of the beams (i.e. the width of the beam is greater than its height). The least resistance to movement would be along the z -axis as it would be resisted by the transverse bending stress of the beams. Therefore, the free comb of the VCDA would be highly sensitive along the z -axis, less sensitive along the y -axis, and least sensitive along the x -axis.

The novel flexure mechanism suggests that by splitting each beam of the two beams that supports the conventional VCDA into two equal halves along the z -axis and placing each pair along each horizontal axis (x,y), a symmetric and relatively high in-plane stiffness would be achieved (see Figure 2.2(b)). All four beams have the same height and length, but have different width; meaning that the stiffness in the z -axis would be maintained to be the same as the z -axis stiffness in the two-beam configuration. But the in-plane stiffness would be increased in the four-beam configuration comparing to the two-beam configuration.

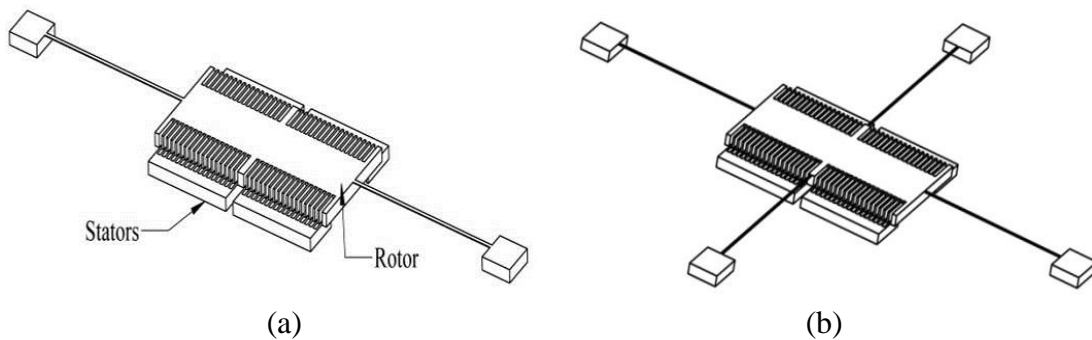


Figure 2-4. Schematics of (a) Two-beam conventional VCDA. (b) Four-beam configuration of the novel VCDA.

This four-beam flexure mechanism has been further pursued to design a 3-DOF MEMS actuator by adding comb fingers along y -axis similar to the fingers along x -axis as shown in Figure 2-5. These added fingers allow the actuator to be rotated about the y -axis too. However, the angle of rotation (about the x and y axes) of the four-beam configuration is less than the angle of rotation of the two-beam (about x -axis) which is due to the high torsional stiffness in the four-beam configuration.

Based on this concept of the flexure mechanism and by trying to achieve a high in-plane stiffness compared to the z -axis stiffness, a number of designs could be explored. These configurations include: three-beam and four-beam configurations with circular fingers as illustrated in Figure 2-5.

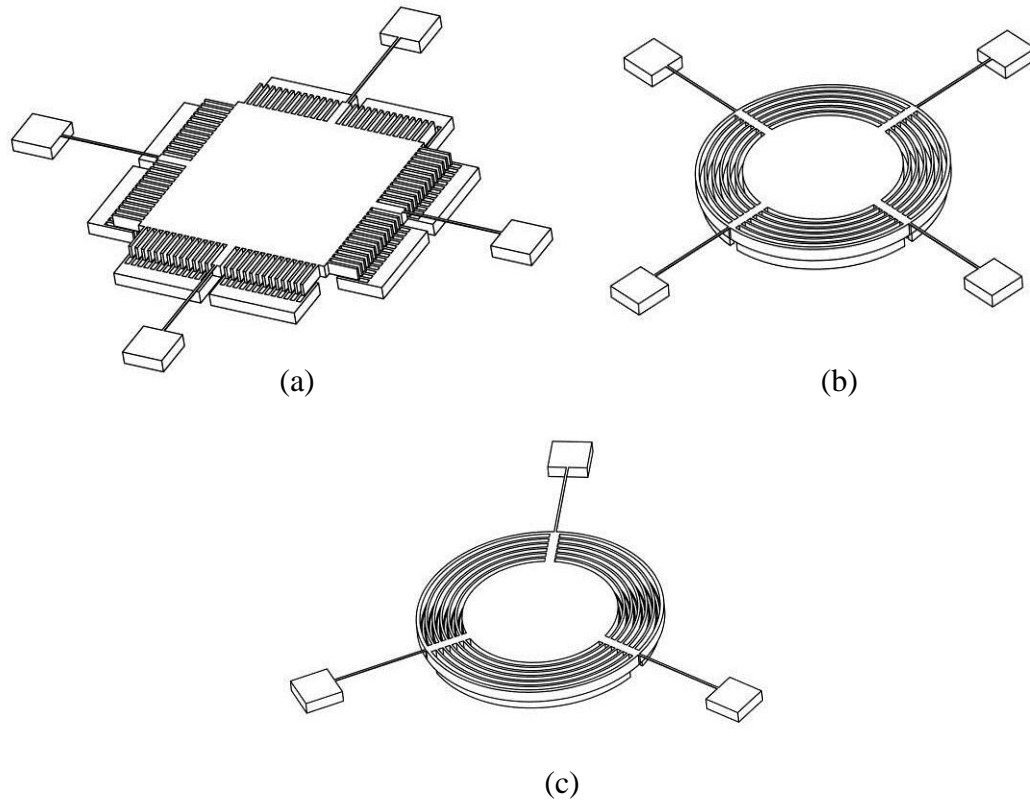


Figure 2-5. Schematics of (a) Four-beam VCDA. (b) Four-beam VCDA with circular fingers. (c) Three-beam VCDA with circular fingers.

The main advantage of the 3-DOF electrostatic actuator is the utilization of the total electrostatic forces that is generated across the electrodes to be directly the driving force on a mass load such as a lens or a deformable micromirror. This is unlike other designs where a stroke magnification

platform is used to transmit the force generated in the actuators to the load while enhancing the stroke of the load. This results in a lower stiffness along the z-axis and a smaller force driving the load. The various angular MEMS angular VCDAAs developed previously compromise the output force during the magnification of the stroke.

2.4. Validation of the Concept

To validate the concept of the novel flexure mechanism, a comparison between a two-beam-configuration and a four-beam configuration were conducted in CoventorWare. Two models were created having the same features; both models have the same z -axis stiffness but different in-plane stiffness.

The first modes of the actuators are shown in Figure 2-6, which confirms that the stiffness along the z -axis in both configurations is the same.

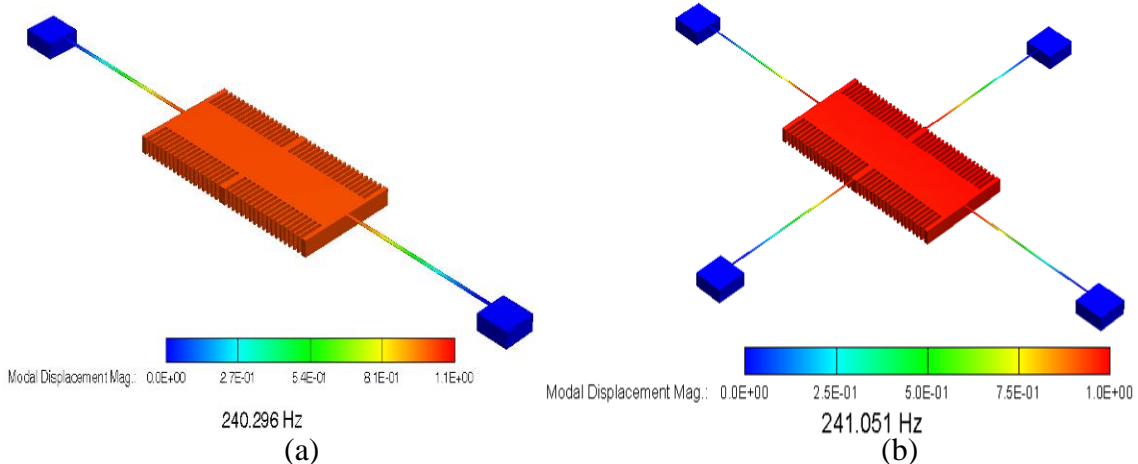


Figure 2-6. First mode for both configurations of the VCDA. (a) two-beam configuration. (b) four-beam configuration.

The static performance analysis showed that the two-beam configuration VCDA achieved a maximum stroke of $9.2 \mu\text{m}$ at a voltage of 30 V (see Figure 2-7(a)). When the input voltage exceeded 30 V , an instability along the y -axis occurred.

The four-beam configuration VCDA achieved almost double the stroke of the two-beam configuration before instability arises, which is $17.2 \mu\text{m}$, at a voltage of 60 V as shown in Figure 2-7(b). When the input voltage exceeded 60 V , an instability along the x -axis took place

before any instability along the y -axis. This is due to the higher electrical force along the x -axis than that along the y -axis because Fe_x develops in the perpendicular direction to the plates of the unit cell capacitance (along g), whereas Fe_y develops in a direction parallel to the plates (fringe field direction).

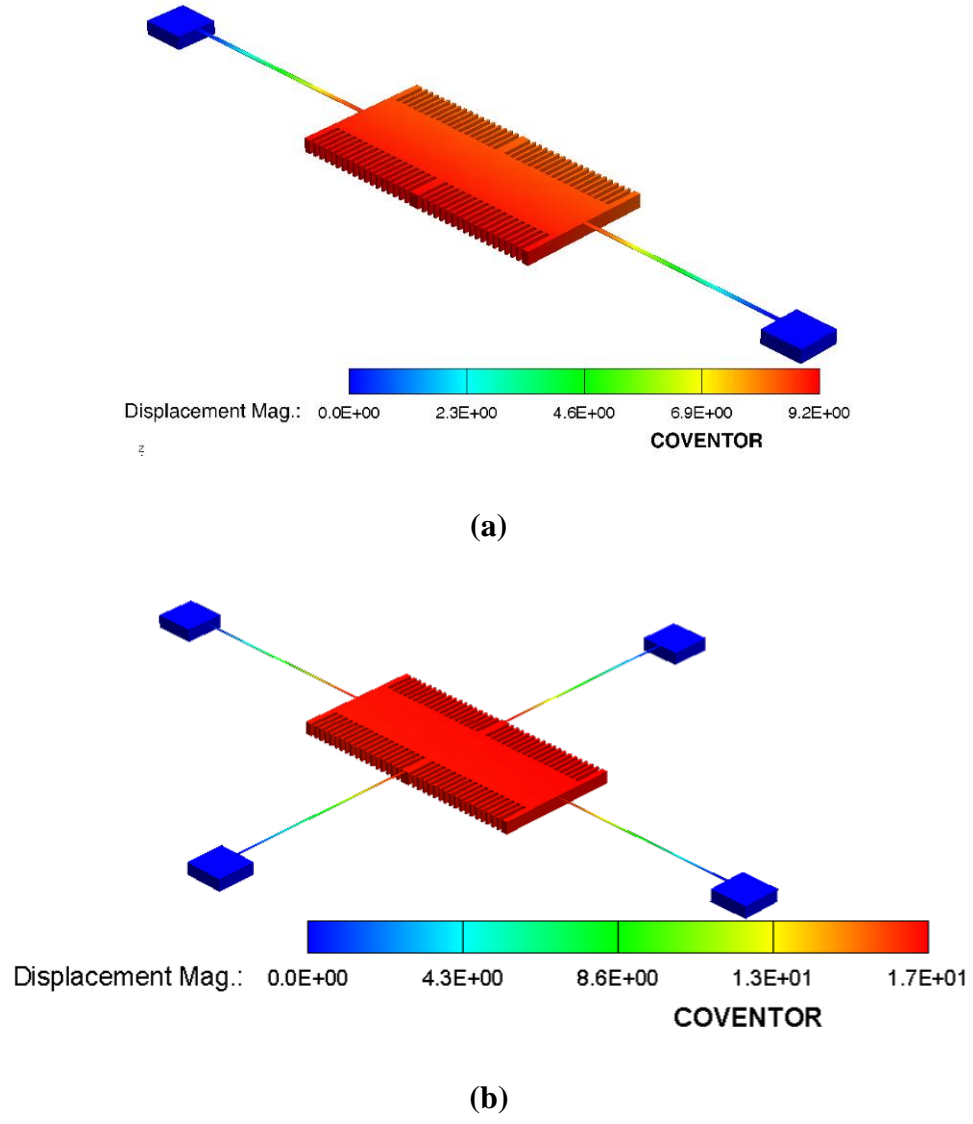


Figure 2-7. Maximum pure translation stroke achieved by both configurations. (a) two-beam VCDA. (b) four-beam VCDA.

2.5. A 3-DOF MEMS electrostatic VCDA

2.5.1. Structure of the Actuator

Two versions of the 3-DOF MEMS electrostatic vertical comb-drive actuator are developed. They are referred to as VCDA 1 and VCDA 2. They are developed such that VCDA 1 is optimized in terms of out-of-plane stroke and rotary motion of the actuator, and VCDA 2 is optimized with respect to output force as it has a wide plate to hold a mass of 3 mg. A three-beam configuration of the actuator with circular fingers was used in both versions.

VCDA 1 consists of a two-layer structure, which includes upper and lower structures. The former contains the rotor (grounded electrodes), and the latter forms three stators (positive electrodes). The lower structure is fabricated in an SOI wafer and contains three stators arranged at 120° , as shown in Figure 2-8 . Each stator consists of arc electrodes that oppose the rotor ring electrodes and they are vertically aligned with them, so that they interdigitate during the actuation. All three stators are electrically isolated from one another. However, electrodes of each stator are electrically connected via the $15 \mu\text{m}$ thickness layer above the Buried Oxide (BOX) layer of the SOI wafer as shown in Figure 2-8. The three circular islands that surround the stators are electrical pads to be used for the wire-bonding of the chip to the external circuit. It is important to highlight that the BOX layer was utilized to provide the electrical isolation between the features of the lower structure.

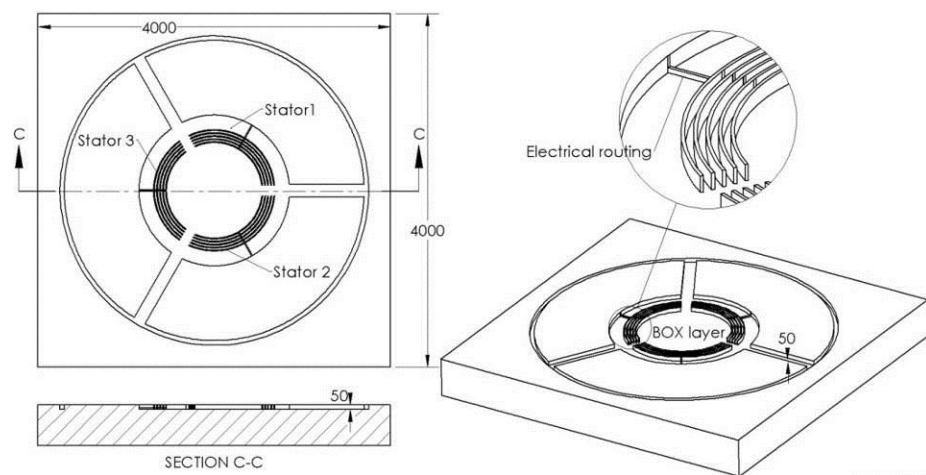


Figure 2-8. Schematics of the stators (lower structure) of the VCDA 1.

The rotor is fabricated in the device layer of another SOI wafer, and it comprises a series of ring electrodes that surround the actuator plate and are attached to it. The ring electrodes, in turn, are attached to the substrate by three supporting beams as shown in Figure 2-9 .

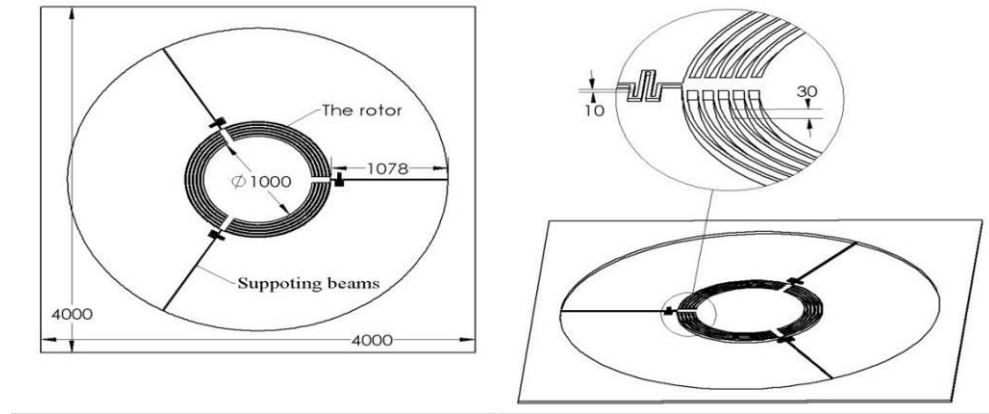


Figure 2-9. Schematics of the rotor (upper structure) of the actuator: top view (left), and isometric view (right).

Both structures are bonded together forming the final structure of the actuator as shown in Figure 2-10.

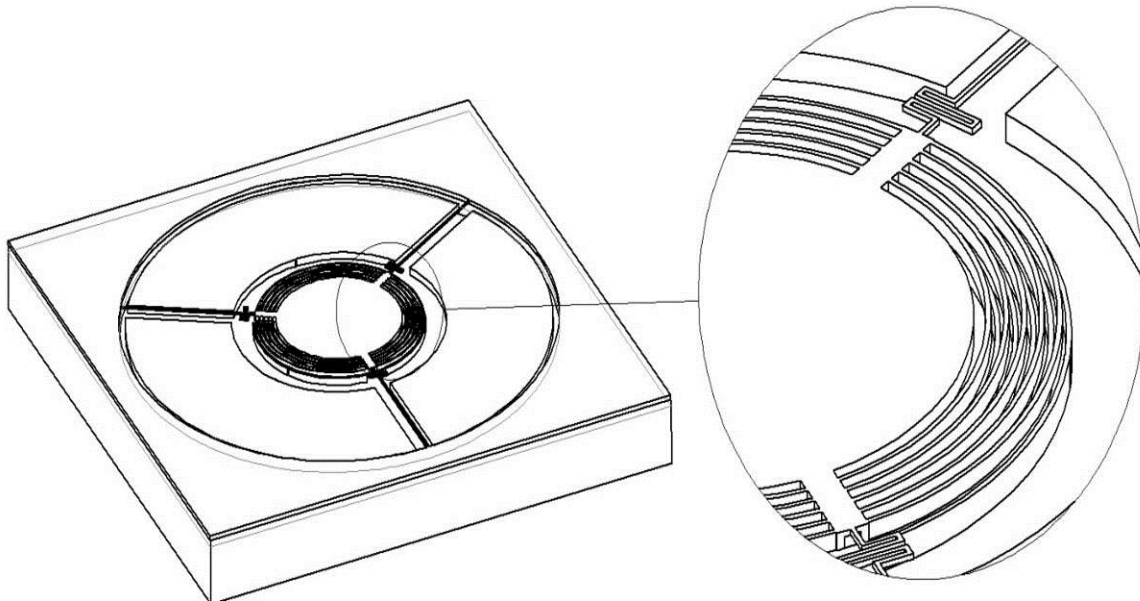


Figure 2-10. Schematic of the 3D model of the 3-DOF MEMS actuator after bonding – VCDA 1.

The following table summarizes the design parameters of VCDA 1.

Design parameter	Value (μm)	Description
w_f	10	Fingers width
h_f	30	Upper fingers height
g	8	Gap between fingers
D_p	1000	Plate diameter
D_{out}	1500	Diameter of outer ring fingers
V	4000x4000x580	Actuator size

Table 2-1. Specifications of VCDA 1.

2.5.2. Principle of Operation

Translation Mode

When a voltage is applied across the negative and positive electrodes, an electrostatic force develops between each pair of adjacent electrodes in the z direction. This electrostatic force moves the rotor (the free upper structure) from its static position down towards the stators (fixed lower structure). When the voltage drops, the rotor moves back to its equilibrium position due to the restoring force in the supporting cantilever beams

Rotation Mode

When a voltage is applied across the rotor and only two stators, the plate of the actuator rotates. This rotation is proportional to the amount of the voltage applied. In the case of actuating only one stator, the rotation angle is less than the angle in the case of actuating two stators at the same voltage. This will be demonstrated through simulations and experimental testing. The actuator plate can be rotated about both the x and y axes.

2.5.3. Finite Element Analysis (FEA)

2.5.3.1. Translation Mode Analysis

Static and dynamic performance analyses were conducted on the 3D model of the actuator in CoventorWare as shown in Figure 2-11. The static analysis is conducted using the CoSolveEm module that runs by iterating between the electrical analysis module (MemElectro) and the mechanical module analysis (MemMech). For dynamic analysis, the HarmonicEM module was used to perform the coupled electromechanical analysis in the frequency domain.

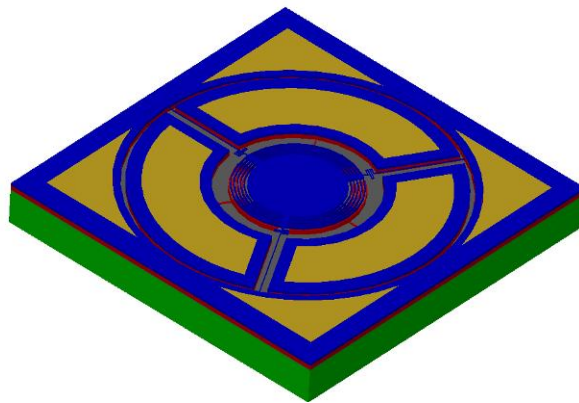


Figure 2-11. CoventorWare 3D model of the VCDA 1

Static Analysis

The bottom face of the 3D model was selected to be a mechanical boundary condition (fixed face) in MemMech, whereas in the MemElectro module, all three stators were selected to be the positive electrode ($V+$) and the rotor was grounded ($V=0V$).

A maximum stroke of 25 μm was achieved at input voltage of 70 V as shown in Figure 2-12.

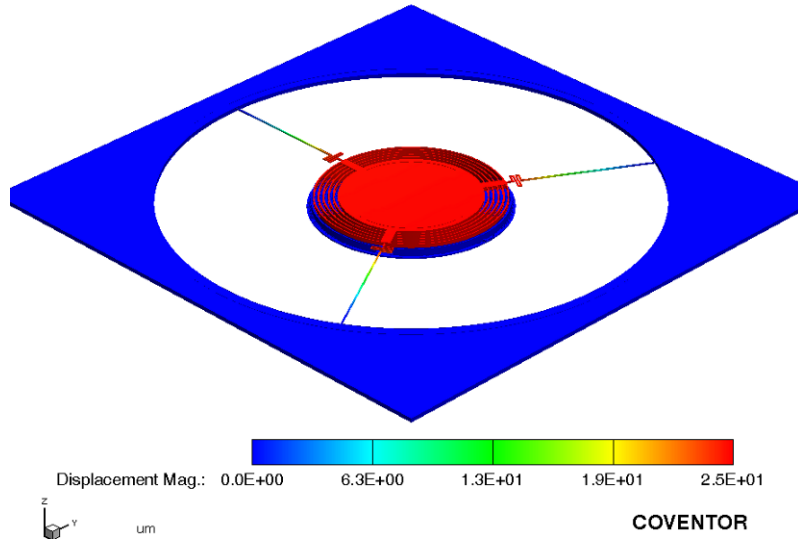


Figure 2-12. Maximum vertical translation stroke of VCDA 1 at 70 V.

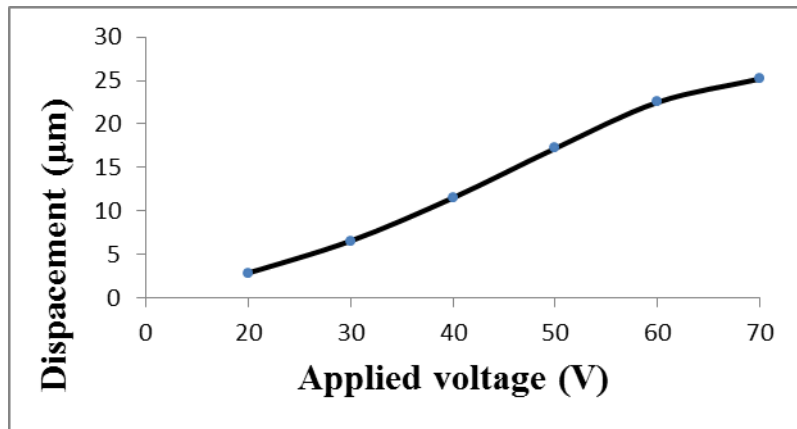


Figure 2-13. Displacement versus voltage of VCDA 1.

The modal analysis of the device was conducted using the MemMech module, and the first three modes of the actuator were 959, 2553, and 2560 Hz; which indicate a high stiffness in the x - y plane, and low stiffness in z -axis.

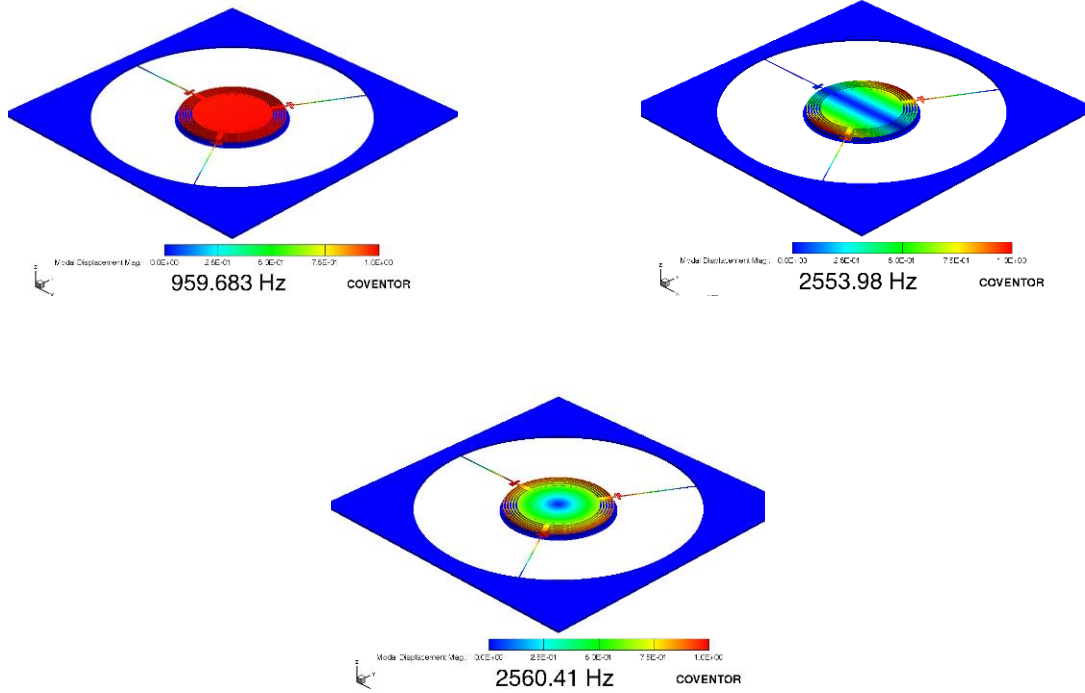


Figure 2-14. First three modes of VCDA 1. (a) First mode: 959 Hz. (b) Second mode: 2553 Hz. (3) Third mode: 2560 Hz.

Dynamic Analysis

The dynamic analysis was conducted on a 3D model of the actuator to investigate its frequency response by applying a combination of sinusoidal input voltage of 10 V in amplitude at various frequencies and a DC input voltage of 30 V to the model. Small damping was assumed ($\xi = 0.1$) in the HarmonicEM module. Thirty frequencies were used in conjunction with the sinusoidal input signal input voltage that range from 1 Hz to 1500 Hz.

The frequency response of the system is shown in Figure 2-15. It was observed from the Bode plot that the natural undamped frequency of the system was 959 Hz, and the bandwidth was 1400 Hz at -3 dB cut-off criterion.

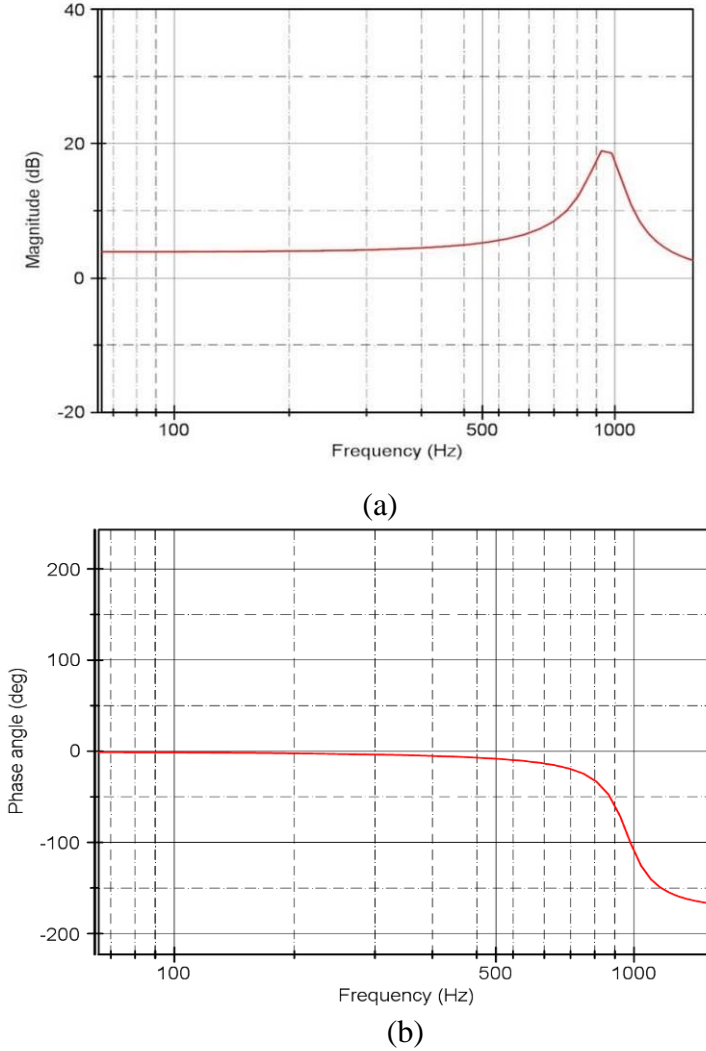


Figure 2-15. The dynamic performance of VCDA 1 in the frequency domain. (a) Magnitude response. (b) Phase response.

2.5.3.2. Rotation Mode Analysis

In the static Analysis of the rotation mode, a DC input voltage was applied across only two stators ($V_1=V_2=V_{in}$, $V_3=0$) and the rotor (0V). A maximum angular stroke of $26 \mu\text{m}$ corresponding to a rotation angle of 0.55° was achieved at an input voltage of 70 V. This is shown in Figure 2-16. The simulation results of the static analysis are shown Figure 2-17.

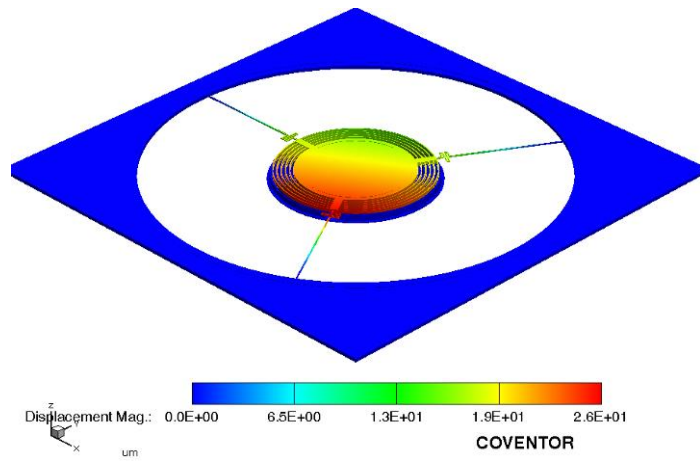


Figure 2-16. Maximum angular stroke of the simulated model of VCDA 1 at 70 V.

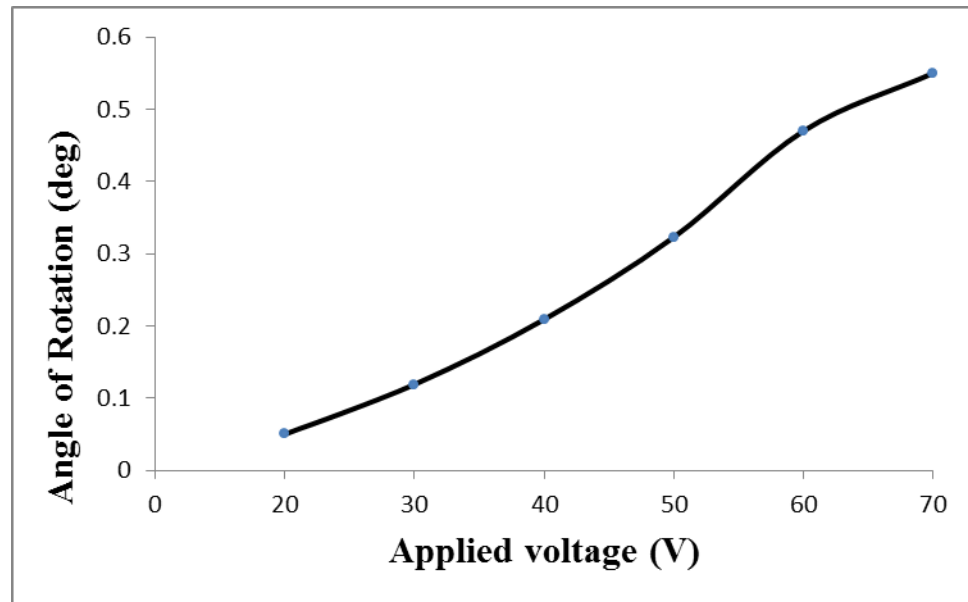
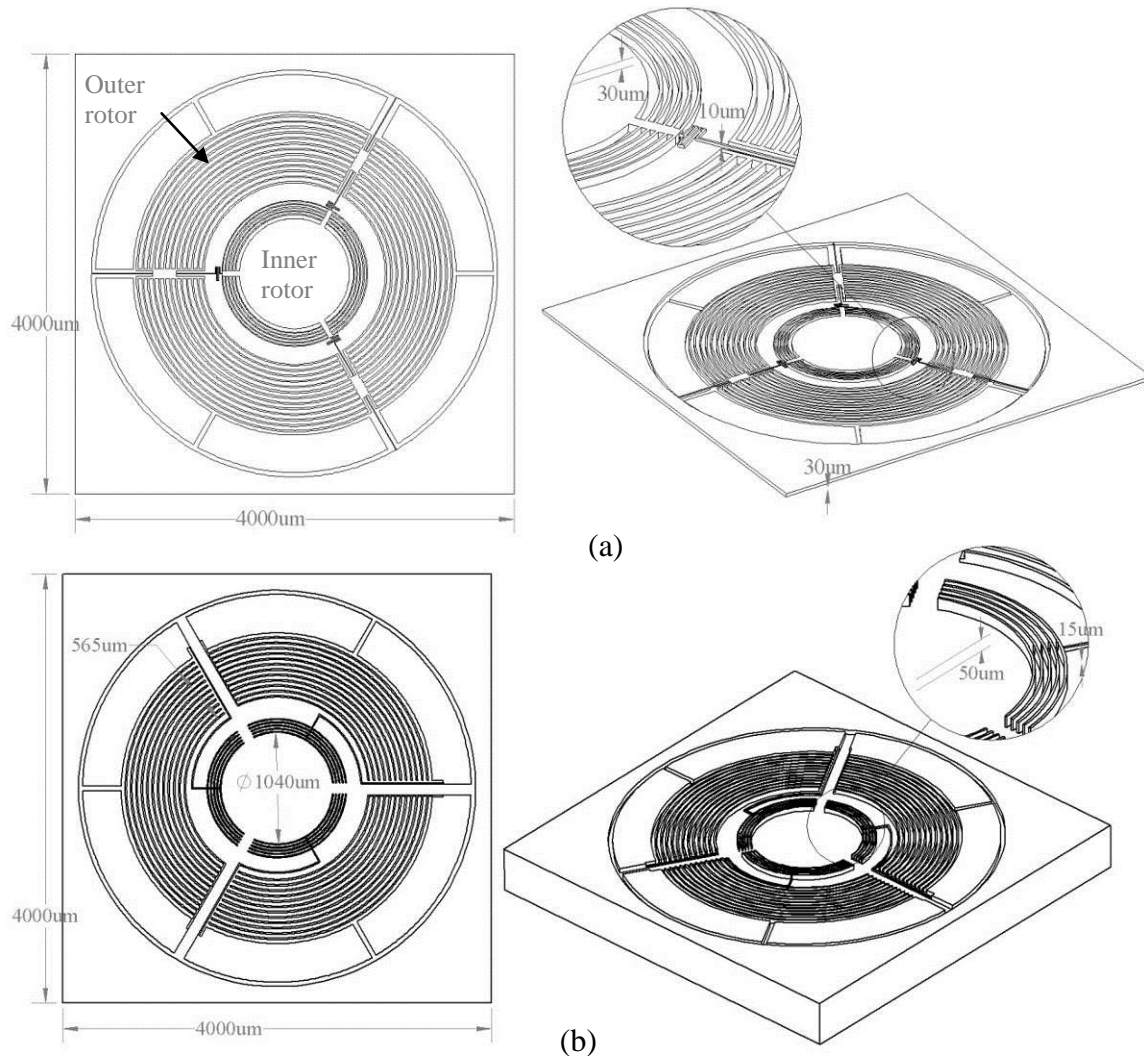


Figure 2-17. Angle versus applied voltage for VCDA 1 in the rotation mode.

2.6. Version 2 of the 3-DOF MEMS Electrostatic VCDA

The second version of the 3-DOF MEMS electrostatic vertical comb-drive actuator, referred to as VCDA 2, is presented and analyzed through numerical simulations in this subsection. This version was optimized with respect to the output force and designed to carry two loads: inner and outer. The former is to be rotated and the latter is to be translated, see Figure 2-18(a). The structure of VCDA 2 is similar to that of VCDA 1, except that it has two rotors as opposed to one rotor. This is shown in Figure 2-18.



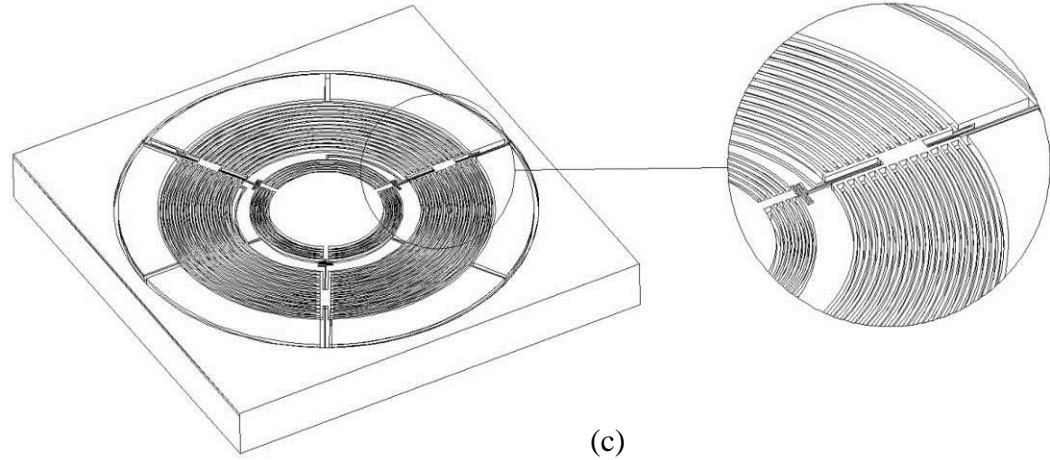


Figure 2-18. Schematics of VCDA 2. (a) Rotors. (b) Stators. (c) Final structure of the actuator with both rotor and stators.

The following table summarizes the dimensional parameters of VCDA 2.

Design parameter	Value (μm)	Description
w_f	10	Fingers width
h_f	30	Upper fingers height
g_{in}	5	Gap between the fingers of the inner rotor
g_{out}	10	Gap between the fingers of the outer rotor
D_p	1040	Plate diameter
Wr_{in}	130	Radial width of the inner rotor
Wr_{out}	565	Radial width of the outer rotor

Table 2-2. Specifications of VCDA 2.

Finite Element Analysis (FEA)

A 3D model of VCDA 2 was also simulated in CoventorWare. The static and dynamic analyses of VCDA 2 were only conducted for the translation motion of the outer rotor. This is in view of the fact that it is developed in order to test the output force of the actuator to translate a 3 mg lens.

Static Analysis of the Translation of the Outer Rotor

The bottom face of the 3D model was selected as a fixed mechanical boundary condition in MemMech, whereas in the MemElectro module, the bottom electrodes of the three outer stators were selected to be the positive electrodes ($V+$), and the rotor and the inner three stators were grounded.

The modal analysis of the device was conducted using the MemMech module, and the first mode of the actuator was a translation along the z -axis coupled with small amount of rotation about the x -axis. This can be seen from the gradual change in the red color in the modal analysis obtained from simulation using CoventorWare that is shown in Figure 2-19. This undesired rotation is attributed to the high stiffness of the outer beams as they have squared cross sections and a shorter length compared to those of the VCDA 1, and it is also attributed to the asymmetric stiffness along the y -axis due to asymmetry of the three-beam configuration. However, the angle of rotation is relatively small, less than 0.01° , so it can be neglected.

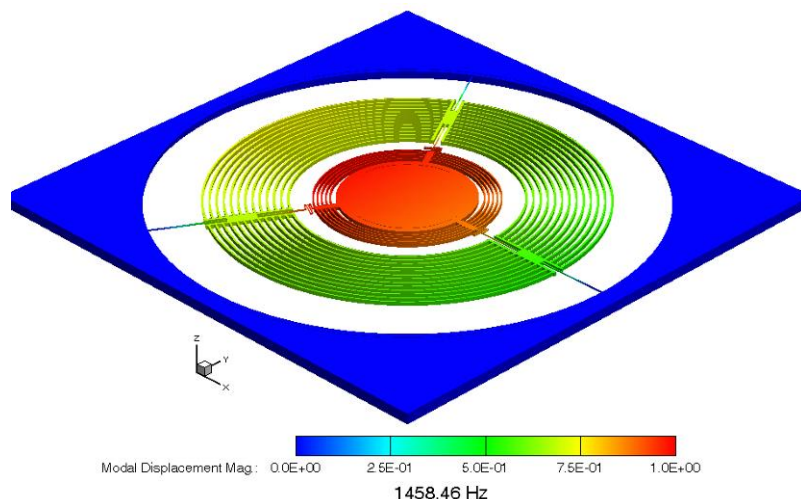


Figure 2-19. Simulation of the first mode of VCDA 2.

A maximum stroke of 9.2 μm was achieved at an input voltage of 50 V as shown in Figure 2-20, and the simulation results of the static analysis are plotted in Figure 2-21.

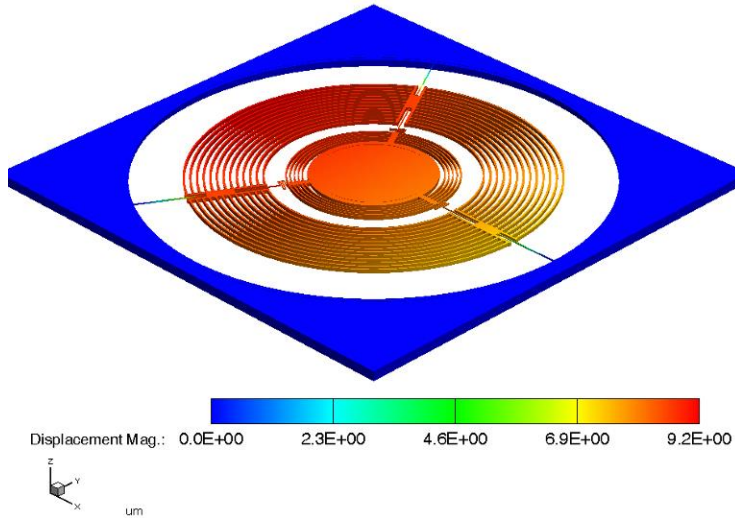


Figure 2-20. Maximum vertical stroke of simulated model of VCDA 2 at 50 V.

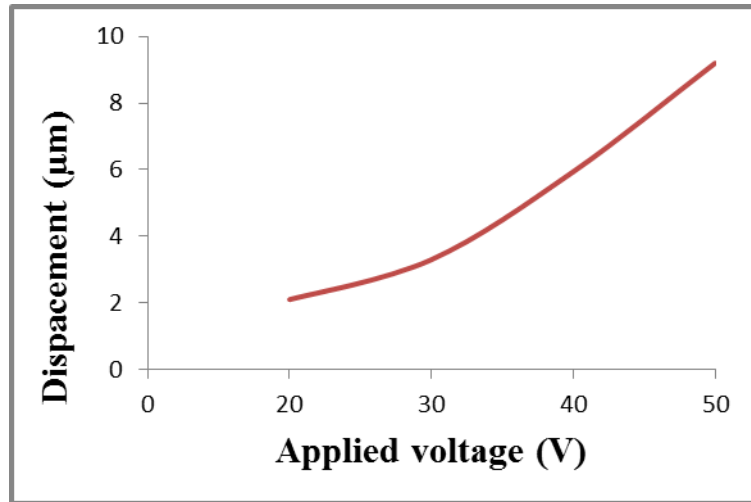


Figure 2-21. Translation stroke of the outer rotor of VCDA 2.

Dynamic Analysis

The dynamic analysis was conducted on the 3D model of the actuator to investigate the frequency response of the actuator by applying a combination of sinusoidal input voltage of 10 V and a DC input voltage of 40 V to the model. Fifty frequencies of the sinusoidal input voltage

were chosen, ranging from 1 Hz to 3000 Hz. The damping in the system was also assumed to be small ($\xi = 0.1$) in the HarmonicEM module.

The frequency response of VCDA 2 is shown in Figure 2-22. It was observed from the Bode plot of the response that the natural undamped frequency of the system is 1440 Hz, and the bandwidth was 2240 Hz.

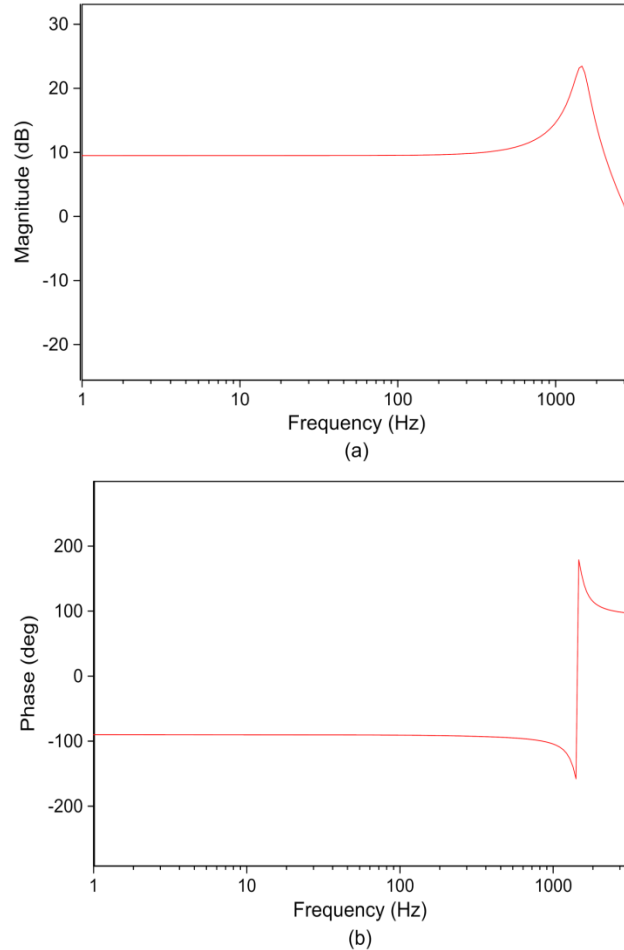


Figure 2-22. Simulations of the dynamic performance of outer rotor of VCDA 2 in the frequency domain. (a) Magnitude response. (b) Phase response.

Chapter 3

Applications of the Novel 3-DOF MEMS Electrostatic VCDA

Auto-focus (AF) and Optical Image Stabilization (OIS) in phone cameras require a high speed response, low power consumption, small size, and a large translational stroke lens actuator. The actuator also has to provide a rotational motion in order to stabilize the image and produce quality images. As explained in the literature, many actuation methods have been used over the past decades to achieve these requirements. One of the incumbent methods is electromagnetic actuation using voice coil motors. Electromagnetic actuators are known to have a number of disadvantages such as high power consumption, slow response and a large size. Piezoelectric actuation is also one of the current methods used to achieve autofocus; nevertheless, piezo actuation suffers from motion control degradation [1][2][38].

Electrostatic actuation potentially offers significant performance characteristics which meet the required features of the lens actuator, including high speed response, low power consumption, small size, and low cost. Currently, only DOC's MEMS electrostatic actuator is used to achieve auto-focus in phone cameras. It uses the principle of single lens motion which requires only an 80 μm travel stroke to achieve the auto-focus as opposed to other approaches which require the entire lens barrel to travel a stroke of 250 μm ; however, such a design is known to have disadvantages such as a complex fabrication process of the actuator and the presence of an undesired lens tilt [1][8]

Two versions of the 3-DOF MEMS electrostatic vertical comb-drive actuator were developed to be used for AF and OIS; they are referred to as the AF actuator and the OIS actuator. The novel AF and OIS actuators would alleviate the disadvantages of DOC's MEMS electrostatic AF and OIS actuators and those of other actuation methods such as electromagnetic and piezoelectric actuators.

The following is a list of the features offered by the novel AF actuator:

- 1- Small size actuator: > (8.4x8.4x0.8) mm
- 2- Low power consumption: < 1mW

- 3- Fast speed response: < 10 ms
- 4- Travel stroke of 3 mg lens: 80 μm
- 5- Easy control method
- 6- Simple to fabricate (customized standard fabrication process)

Similarly, the following is a list of the features of the OIS actuator:

- 1- Actuator size: (12.6x12.6x1) mm
- 2- Low power consumption: < 1mW
- 3- Response speed: < 20 ms
- 4- Entire camera module rotation technique: module mass is 560 mg
- 5- Rotation angle : 0.6 °
- 6- Easy control method
- 7- Simple to fabricate

3.1. AF Actuator

3.1.1. Structure of the Actuator

A MEMS Electrostatic Vertical Comb-drive Actuator for Autofocus is developed to meet the autofocus requirements in phone cameras. It utilizes only one degree of freedom of the novel 3-DOF MEMS electrostatic actuator, i.e. pure translational motion. The actuator consists of a two-layer structure: upper and lower. The former forms the rotor (grounded electrodes), and the latter forms the stators (positive electrodes).

The lower structure, illustrated in Figure 3-1, contains the stators which comprise a set of electrically connected electrodes. The stators are fabricated in a device layer of a bottom SOI wafer, and the BOX layer is utilized to provide the electrical separation between the rotor and the stators.

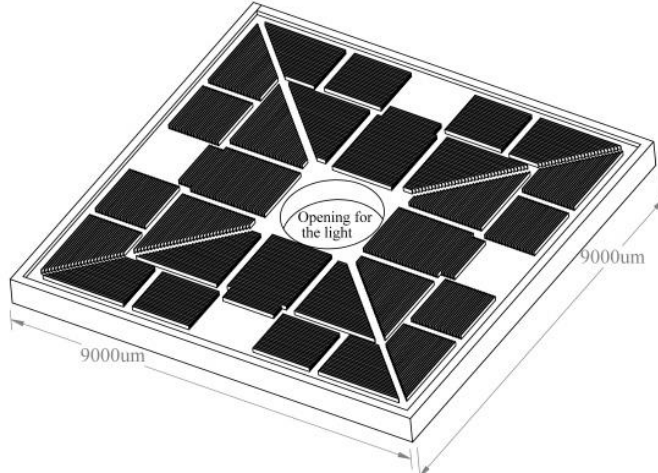


Figure 3-1. Schematics of the stator (lower structure) of the AF actuator: top view (left) and isometric view (right).

The rotor, upper structure, is attached to the substrate using four supporting serpentine beams as shown in Figure 3-2. A lens of mass of 3 mg would be integrated into the central ring of the rotor.

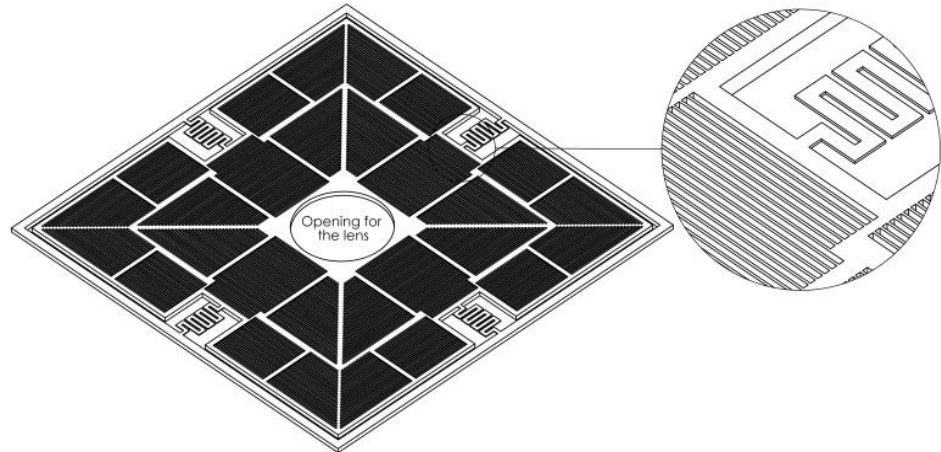


Figure 3-2. Schematics of the rotor (upper structure) of the AF actuator.

By bonding both structures, the upper structure electrodes would be adjacent to the lower structure electrodes, so that they interdigitate during the actuation. The 3D model of the final structure of the AF actuator is illustrated in Figure 3-3.

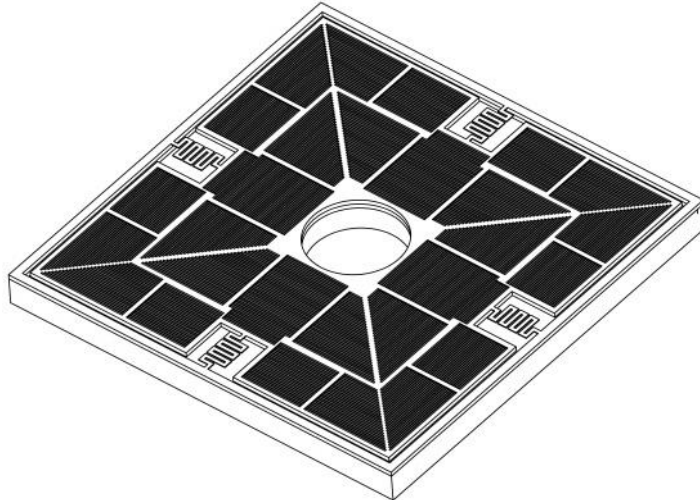


Figure 3-3. Schematic of 3D model of the AF actuator after bonding.

The following table lists the specifications of the AF actuator:

No	Features	Specifications
1	Actuator size	(9x9x7) mm
2	Gap between the adjacent fingers (g)	8 μm
3	Finger width (w_f)	15 μm
4	Upper SOI wafer thickness	Device layer: 100 μm , handle layer: 500 μm , buried oxide: 5 μm
5	Bottom SOI wafer thickness	Device layer: 100 μm , handle layer: 500 μm , buried oxide: 5 μm
8	Mass of Lens	3 mg

Table 3-1. Specifications of the novel AF actuator

3.1.2. Principle of Operation

When a voltage is applied across the rotor and the stators, an electrostatic force develops between each pair of adjacent electrodes. This electrostatic force moves the rotor from its static

position down towards the stators. The upper structure moves back due to the restoring mechanical force in the supporting serpentine beams.

The requirement of the AF actuator is to translate a 3 mg lens barrel within a range of 80 μm in pure translation to achieve the focus of the image from 10 cm position to infinity.

3.1.3. Finite Element Analysis (FEA)

A 3D model of the actuator was simulated in CoventorWare. Due to the symmetry, only one quarter of the actuator was modelled. The boundary conditions (Symmetry Planes) were set in the MemMech module for the walls of the middle mass, see Figure 3-4. The static and dynamic analyses were conducted using the Co-solve and Harmonic modules, respectively.

The static analysis results showed that the actuator achieved a maximum stroke of 78 μm at a voltage of 70 V. The simulation results of the pure translational stroke of the actuator corresponding to different values of DC input voltage are plotted in Figure 3-5. Based on these results, the actuator is achieving the required stroke for auto-focusing.

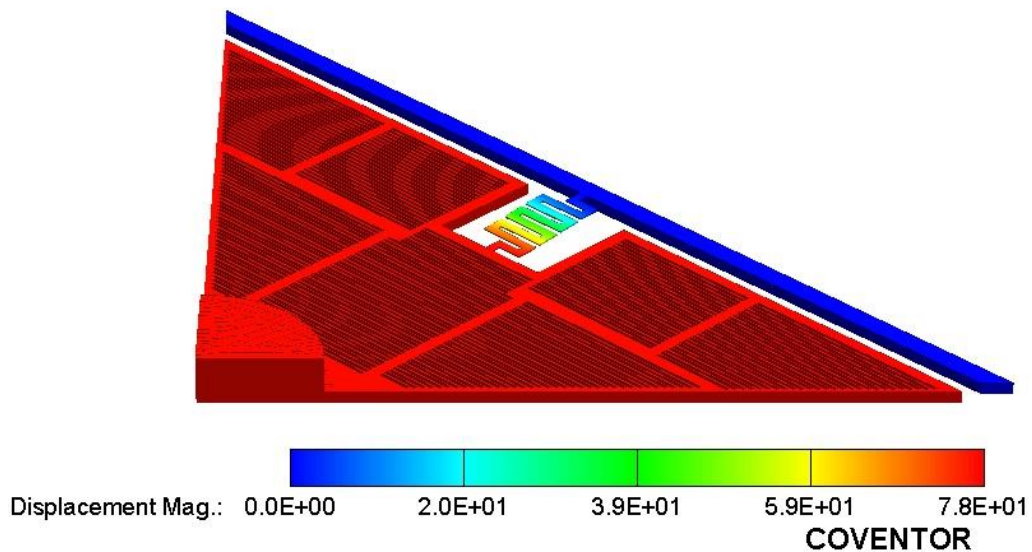


Figure 3-4. Maximum translation stroke of the AF actuator holding a mass of 3 mg at 70 V.

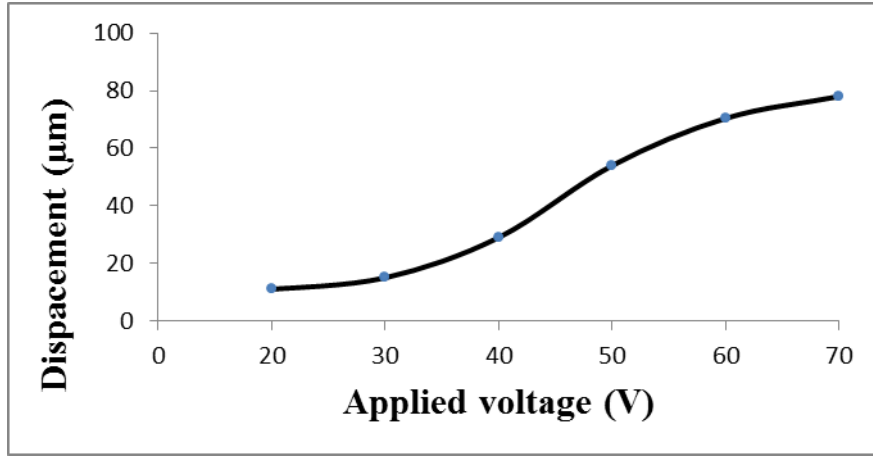


Figure 3-5. Displacement versus voltage for the AF actuator.

In the dynamic analysis, a small damping ratio (ξ) of 0.1 was assumed, and the simulation was conducted in the frequency domain. The simulation results of the dynamic response show that the actuator has an undamped natural frequency at 430 Hz, and the bandwidth was 670 Hz as shown in Figure 3-6.

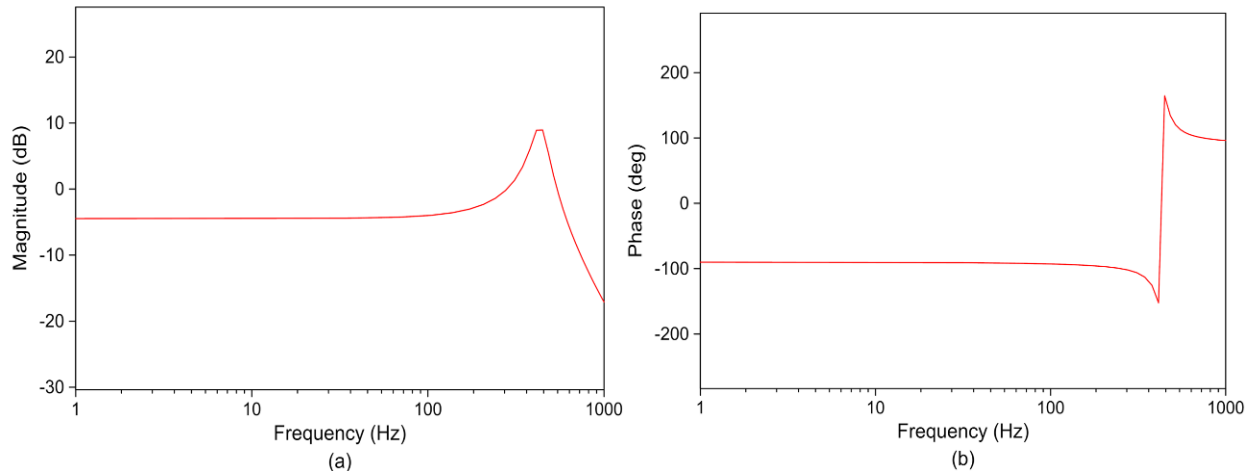


Figure 3-6. Dynamic performance of the AF actuator in the frequency domain. (a) Magnitude response. (b) Phase response.

3.2. OIS Actuator

3.2.1. The Structure of the Actuator

As previously discussed, there are three main techniques to achieve OIS in phone cameras. The three techniques are the lens shift-based OIS, the sensor shift-based OIS, and the entire module rotation OIS. The best OIS method among these technologies is the entire module rotation as it compensates not only for the linear movement of the hand (i.e. hand shake), which is the case of the first two techniques listed above, but also for yaw and pitch rotations of the hand, which have the most negative impact on the image quality. The following are requirements of the OIS actuator based on discussion in the literature:

- 1- Angle of rotation of the actuator to compensate for human hand shaking is 0.6° .
- 2- Response speed of the actuator is < 20 ms.

A MEMS Electrostatic Actuator for optical image stabilization is developed to meet the latter requirements for stabilized image using the entire module rotation technique. The design of the novel OIS actuator utilizes only two degrees of freedom of the 3-DOF MEMS electrostatic vertical comb-drive actuator presented in Chapter 2. These motions are the rotations about the x and y axes (yaw and pitch rotations). The actuator consists of a two-layer structure: upper and lower. The free upper structure forms the rotor, as illustrated in Figure 3-7.

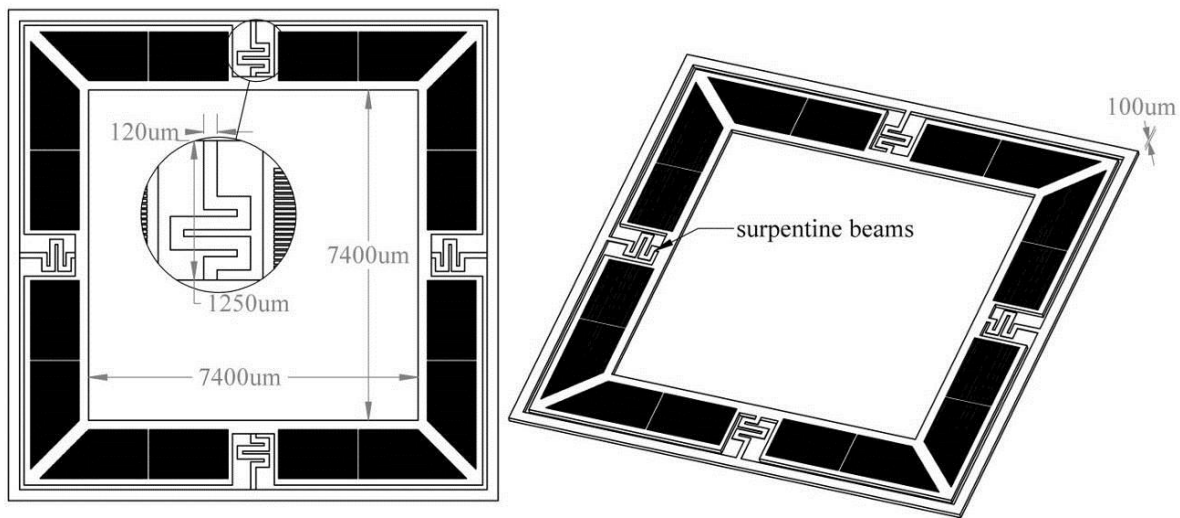


Figure 3-7. Schematics of the rotor (upper structure) of the OIS actuator: top view (left) and isometric view (right).

The lower structure forms 8 stators (each two neighboring sets of fingers are forming 1 stator), which are electrically isolated to enable the user to control the rotations of the entire module of the camera as illustrated in Figure 3-8. The BOX layer in the bottom SOI wafer was utilized to achieve the electrical separation between the stators during the fabrication process. A camera module of 560 mg will be integrated into the squared space at the center of the actuator.

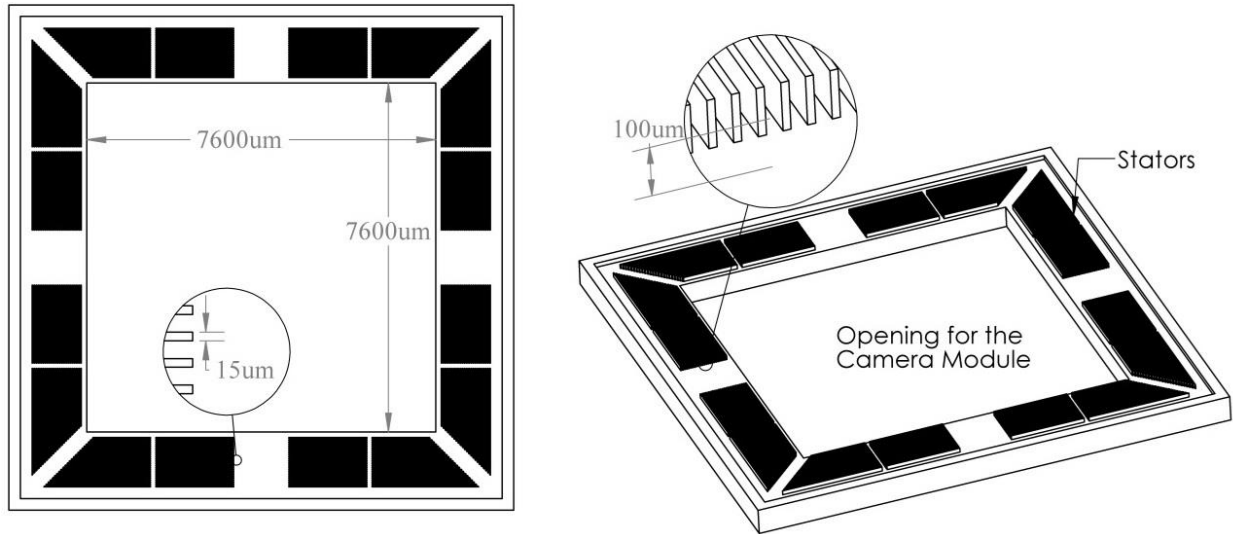


Figure 3-8. Schematics of the stators (lower structure) of the OIS actuator: top view (left) and isometric view (right).

Both structures are bonded together forming the final structure of the actuator as shown in Figure 3-9.

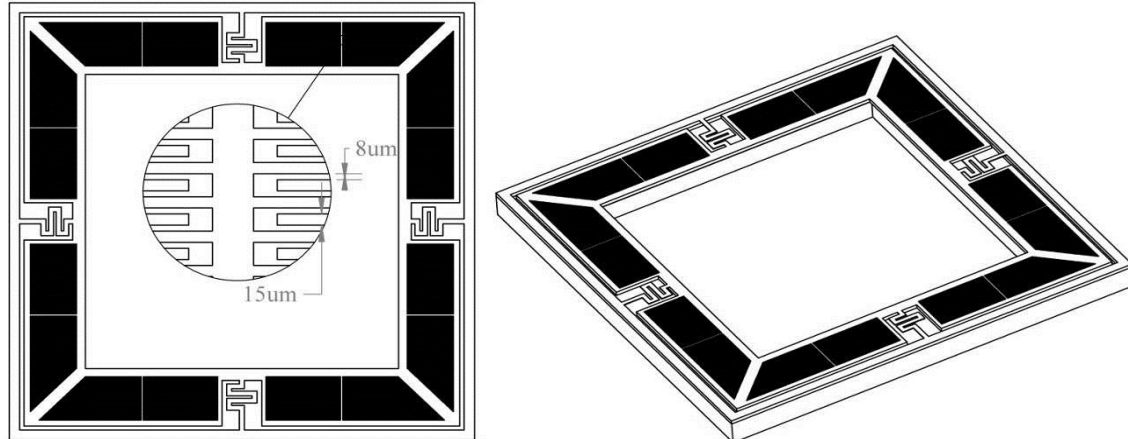


Figure 3-9. Schematic of the OIS actuator after bonding.

The following table lists the specifications and dimensions of the novel OIS actuator.

No	Features	Specifications
1	Actuator size	(12.6x12.6x0.8) mm
2	Gap between the adjacent fingers (g)	8 μm
3	Fingers width (w_f)	22 μm
4	Fingers height (h)	100 μm
7	Camera module size	(7.6x7.6x5) mm
8	Camera module weight	560 mg

Table 3-2. Specifications of the novel OIS actuator.

3.2.2. Principle of Operation

When a voltage is applied across the rotor (ground) and any successive four stators located in each side of the actuator ($V_{in}=V1=V2=V3=V4$ and other stators are grounded), an electrostatic force develops between each pair of adjacent fingers; which, in turn, rotates the rotor from its static position down towards the actuated stators. The rotor moves back to its equilibrium position due to the restoring force in the supporting beams. During the rotation of the rotor, the upper fingers in the rotor will move and misalign with the bottom fingers in the actuated stators; however, due to the large stiffness in the x - y plane, the actuator tolerates a misalignment of up to 0.6° angle of rotation based on the simulation result, as there is no lateral instability threshold that exists within this range.

3.2.3. Finite Element Analysis (FEA)

To predict the static and dynamic performances of the OIS actuator, CoventorWare was also used to assess the performance of the actuator. The simulation results of the angular displacement of the actuator corresponding to different values of DC input voltage are shown in Figure 3-10. The plot indicates a steep increase in the stroke of the actuator between 110 V and 130 V, which might be attributed to a lateral nonlinear force between the walls of the fingers. Therefore, at those values of the input voltage, there are two coupled forces rotating the rotor: one along the z -axis and the other one along the x -axis.

A maximum stroke of 81 μm - corresponding to an angular motion of 0.6°- at an input voltage of 140V was achieved as shown in Figure 3-11.

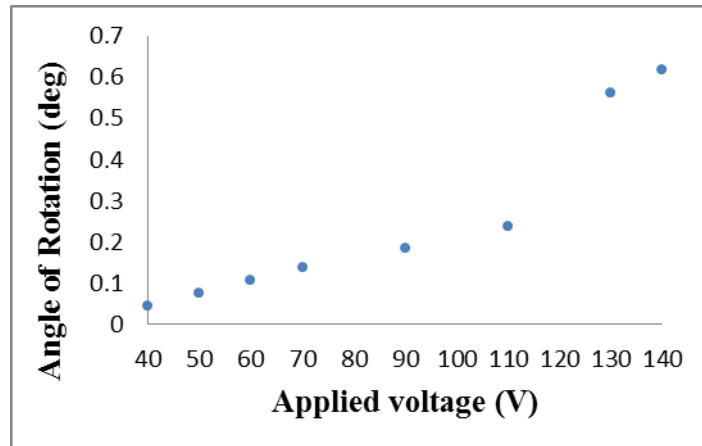


Figure 3-10. Displacement versus voltage of the OIS actuator.

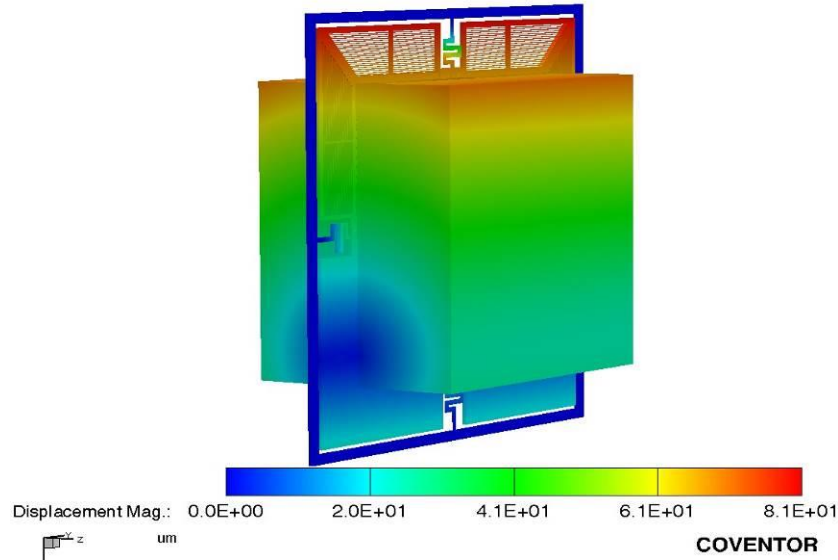


Figure 3-11. Maximum angular stroke of the simulated model of the OIS actuator holding a mass of 560 mg at 140 V.

Figure 3-12 shows the dynamic response of the model of the OIS actuator. The Bode plot shows that the natural frequency of the actuator is 93 Hz and the bandwidth is 110 Hz (- 3dB criterion). These characteristics meet the requirements of the OIS actuator in terms of the required response speed and angle of rotation.

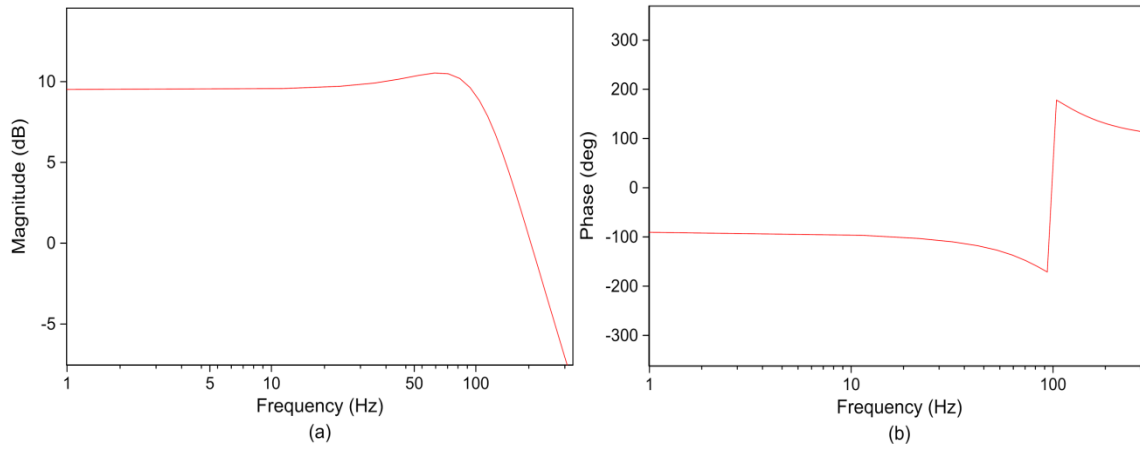


Figure 3-12. Dynamic performance of the OIS actuator in the frequency domain. (a) Magnitude response. (b) Phase response.

Chapter 4

Fabrication Process

VCDA 1 and VCDA 2 were fabricated using the Micralyne All-Silicon Platform (MASP) fabrication process, whereas the AF and OIS actuators were attempted to be fabricated using a modified version of the MASP process. The standard recipe of the MASP fabrication process was not compatible with the specifications of the AF and OIS actuators; therefore, a modified recipe of the MASP process was attempted at the McGill Nano-tools Micro-fab facility.

4.1. Fabrication Process for VCDA 1 and VCDA 2

The Micralyne All-Silicon Platform fabrication process is a recent Direct Reactive Ion Etching (DRIE) bulk micromachining process developed by Micralyne Inc.; both VCDA 1 and VCDA 2 were fabricated in the trial run of this process.

The main advantage of this process is the potential elimination of any misalignment between the upper and lower electrodes as the etching of the upper electrodes is done after the bonding of the wafers, avoiding bonding misalignment (which is in the range of about $5 \mu\text{m}$); whereas in a conventional VCDA fabrication process both upper and lower electrodes are first etched separately and then bonded which results in bonding misalignment.

MASP is a 7 masks process, and it contains DRIE of the two SOI wafers. First, two trenches with different depths are etched in the device layer of the lower SOI wafer (referred to as the Base SOI). One of them is fully etched to the BOX layer, and the other one is partially etched up to a certain depth to allow for electrical routing between the electrodes of the device layer as shown in Figure 4-1(a).

Second, the device layer of the upper SOI wafer, referred to as the Mirror SOI, is also etched from the top side to a certain depth to form the thickness of the beams or reduce the weight of the micromirror plate, see Figure 4-1(b). Both Base and Mirror SOI wafers are bonded using a direct bonding technique, as shown in Figure 4-1(c). The handle layer of the Mirror SOI wafer is then removed, and the bottom side of the device layer of the Mirror SOI wafer is etched through without etching the lower Base SOI device layer as shown in Figure 4-1(d). The goal of this step is to form the features of the upper electrodes in the Mirror SOI device layer.

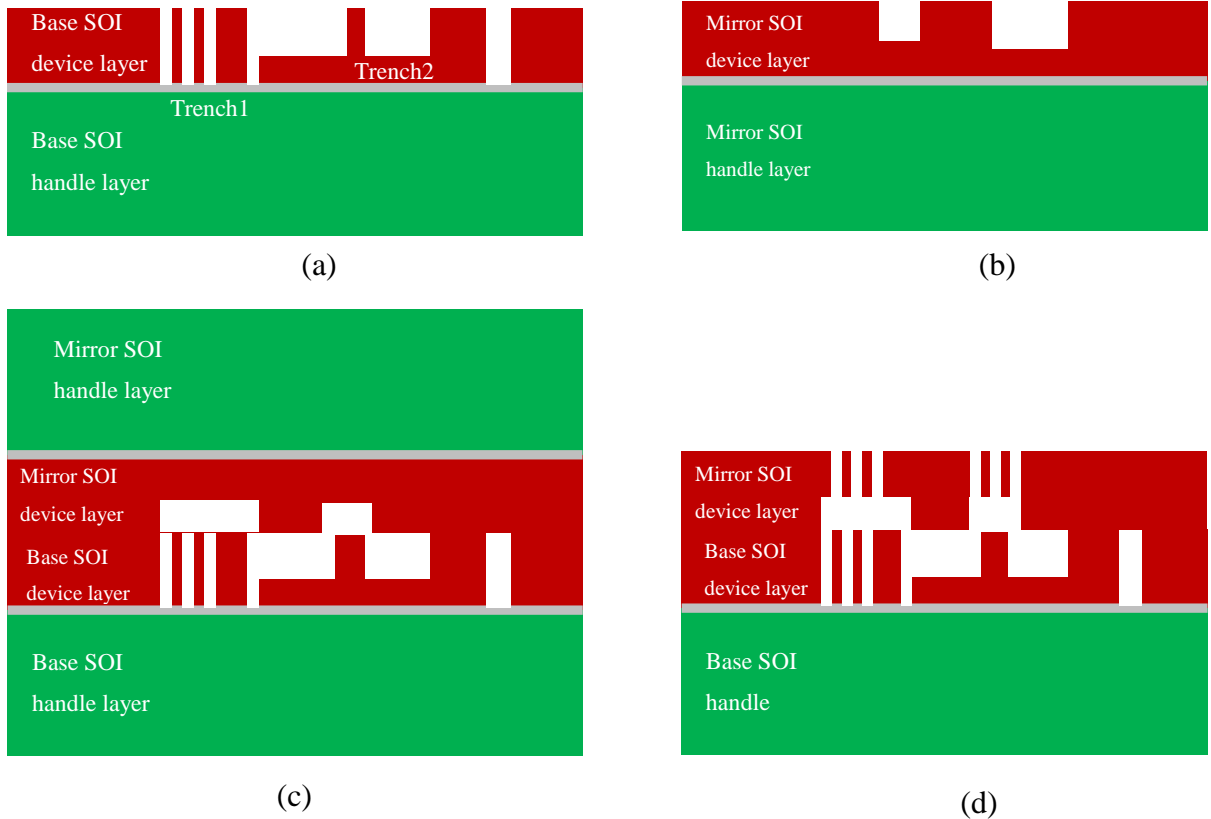


Figure 4-1. The MASP fabrication process. (a) Fabrication of a Base SOI wafer. (b) Fabrication of mirror device layer. (c) Bonding of both SOI wafers. (d) Final structure of the actuator.

The fabricated chips of VCDA 1 and VCDA 2 using the MASP fabrication process are shown in Figure 4-2.

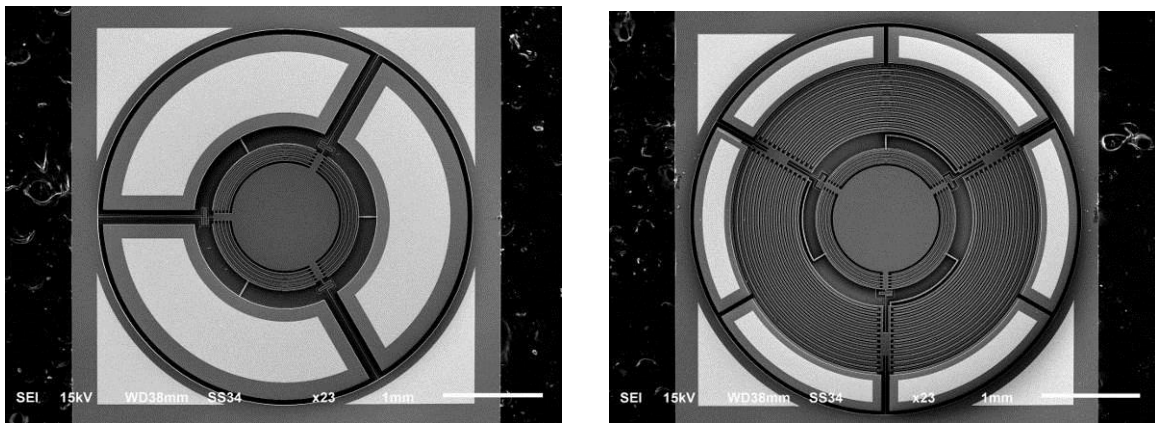


Figure 4-2. SEM micrographs of the VCDA 1 (right) and VCDA 2 (Left) prototypes.

Both devices were inspected using the Scanning Electron Microscope (SEM) to investigate the accuracy of the alignment between the upper and the lower electrodes. Figure 4-3 shows almost perfect alignment between the upper and lower electrodes where the misalignment is less than 0.005% of the gap between the fingers, which is negligible.

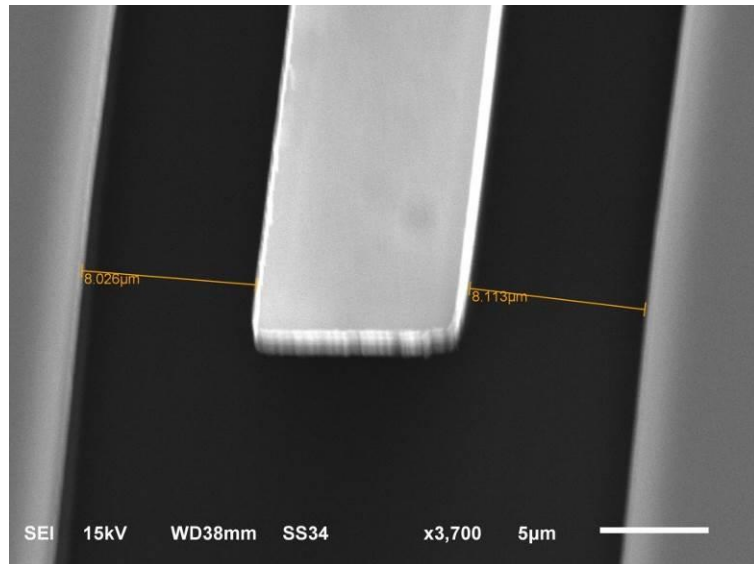


Figure 4-3. SEM micrograph of the gap between adjacent electrodes of the actuator.

The chips were delivered unpackaged from CMC Microsystems Inc.; therefore, they were wire-bonded and packaged at the clean room of the ECTI center at the University of Toronto. Figure 4-4 shows the final wire-bonded and packaged chip.

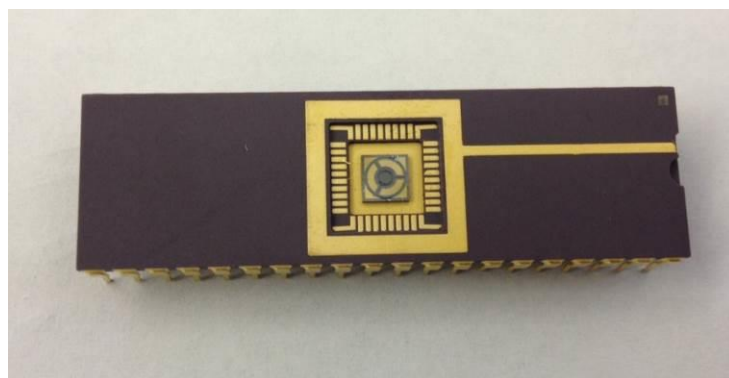


Figure 4-4. Packaged chip of VCDA 1.

4.2. Fabrication Process of AF and OIS Actuators

A customized fabrication process to fabricate the AF and OIS MEMS electrostatic actuators was developed; that is because the design rules of the trial run of the MASP fabrication process - used to fabricate the novel 3 DOF MEMS electrostatic actuator- was not suitable for the OIS and AF actuators. Therefore, a fabrication process similar to the MASP fabrication process but with some changes so that it is suitable for the fabrication of the AF and OIS actuators was developed. The process was initiated at McGill Nano-tools Micro-fab facility, and 8 out of 12 steps of the process were successfully achieved, and the remaining steps were left for future work due to time constraint.

It is important to highlight the differences between the modified MASP and the standard MASP fabrication processes. The first key difference is the thickness of the device layers of the Base (lower structure) and Mirror (upper structure) SOI wafers, where the thickness is 100 μm for both SOI wafers in the modified MASP process and only 50 μm in the standard MASP process.

The second difference is the type of the bonding technique used to bond the Base and Mirror wafers. In the MASP process, a direct Si-Si bonding was used, whereas in the modified MASP process, eutectic wafer bonding is utilized. In the direct Si-Si bonding technique, there are no intermediate layers between the wafers, as they are directly bonded in a furnace at high temperature. In the eutectic bonding, at least two intermediate layers are deposited on one of the wafers prior to bonding; these layer can be Titanium and Gold (Ti/Au), or Germanium and Aluminum (Al/Ge). The advantage of using eutectic bonding is that it can be realized during DRIE of the Mirror device layer as it is used as an etch stop layer to protect the features of the Base device layer. Conversely, in the standard MASP process, the etching of the mirror device layer is time-based, making it the most crucial step in the process. Specifically, if an over etching of more than 1 μm of the Base wafer features occurs, the performance of the comb-drive actuator would be negatively affected.

The third difference, which is the most important one, is the introduction of the pre-engagement between features of the Base and the Mirror wafers; meaning that pre-engagement would be created between the vertical comb-drive fingers. The existence of the pre-engagement would eliminate the drawback of the absence of the pre-engagement of the fabrication process of the most vertical comb-drive actuator [32].

The following table lists the key differences between the standard MASP and modified MASP fabrication processes.

Step	MASP process	Modified MASP process
Thickness of the device layer of the Base SOI wafer (μm)	50	100
Thickness of the device layer of the Mirror SOI wafer (μm)	30	100
Wafer bonding technique	Direct Si-Si bonding	Eutectic bonding
Pre-engagement between the rotor and stators fingers	No	Yes
Ensuring the protection of the features of the base device layer during Mirror device layer etching	No	Yes

Table 4-1. Comparison between the MASP and the modified MASP fabrication processes.

4.3. Modified Recipe of MASP Fabrication Process

The following table contains the detailed fabrication steps of the modified MASP process. It provides a summary of the step, mask layout, cross-sectional view, and isometric view of the 3-D CoventorWare model, and the microscopic picture of the actual process wafer.

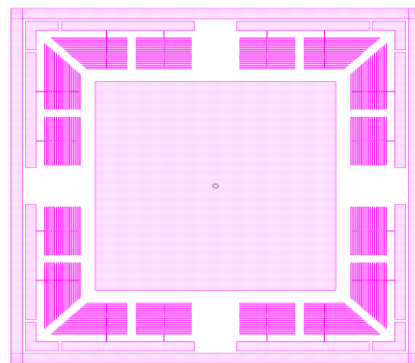
4.3.1. Base SOI Wafer Fabrication (Lower Structure)

(1) SOI wafer							
The process begins with an SOI wafer coated by a Silicon Oxide layer of 700 nm from the bottom side. The thickness of the device layer, buried oxide layer, and handle layer of the SOI are 100 μm , 5 μm , and 500 μm , respectively.	No Mask						
Cross-sectional View							
<p>A cross-sectional diagram of the SOI wafer. It shows three distinct layers. The top layer is red and labeled "100 μm". Below it is a thick green layer labeled "500 μm". The bottom layer is also green. A vertical dimension line indicates the total thickness of the green layers is 500 μm.</p>							
(2) Backside alignment mask patterning							
The bottom Silicon Oxide layer of the Base SOI wafer is photolithographically patterned through a Backside alignment Mask and etched using Reactive Ion Etching (RIE).	<p>Mask 1: Backside alignment</p> <p>A schematic diagram of a backside alignment mask. It consists of a large rectangular frame containing two smaller rectangles, each with a cross-shaped pattern of black lines.</p>						
Cross-sectional View							
<p>A cross-sectional diagram of the SOI wafer after patterning. The bottom silicon oxide layer now features a pattern of small black squares and lines, corresponding to the alignment marks on the mask. The other layers remain unpatterned.</p>							
<table border="1"> <tr> <td> Silicon Oxide</td> <td> SOI device layer</td> <td> PR</td> </tr> <tr> <td> BOX</td> <td> SOI handle layer</td> <td></td> </tr> </table>		Silicon Oxide	SOI device layer	PR	BOX	SOI handle layer	
Silicon Oxide	SOI device layer	PR					
BOX	SOI handle layer						

(3) Trench1 and Trench2 masks patterning

The first mask of Silicon Oxide is deposited on the device layer of the Base SOI wafer, and it is photolithographically patterned through (Trench1). Trench1 defines the lower comb electrodes. The second mask is a PR layer of 10 μm , which is deposited and patterned through (Trench2) mask. The purpose of the patterned two masks (Silicon Oxide and PR) is to etch the silicon device layer of the SOI wafer up to two different depths ($B_1 = 100 \mu\text{m}$ and $B_2 = 85 \mu\text{m}$) in order to provide the electrical separation between device layer regions (stators) from one another by etching B_1 and to allow for electrical routing between the fingers of each stator by etching B_2 .

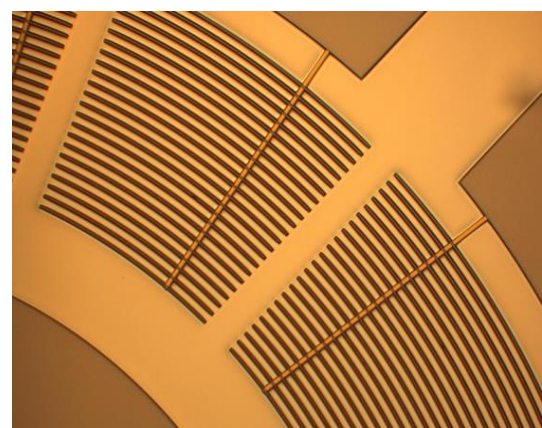
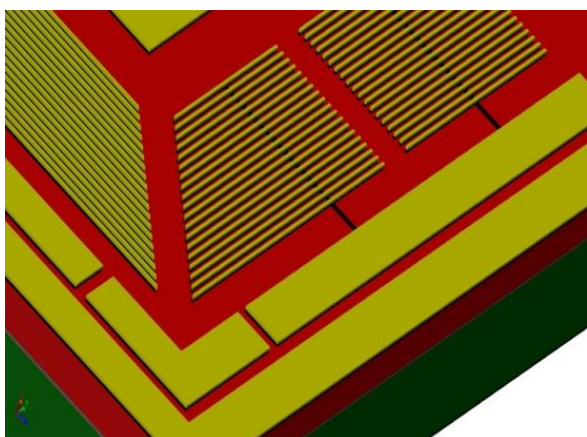
Mask 2: Trench1



Cross-sectional View



CoventorWare 3-D model (left) and microscopic image (right)

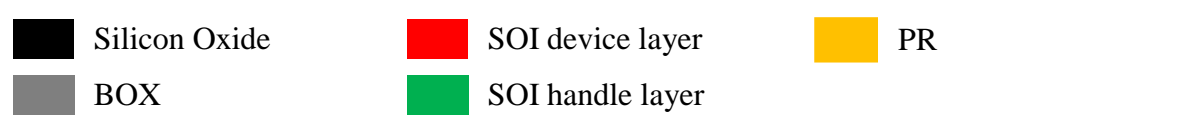
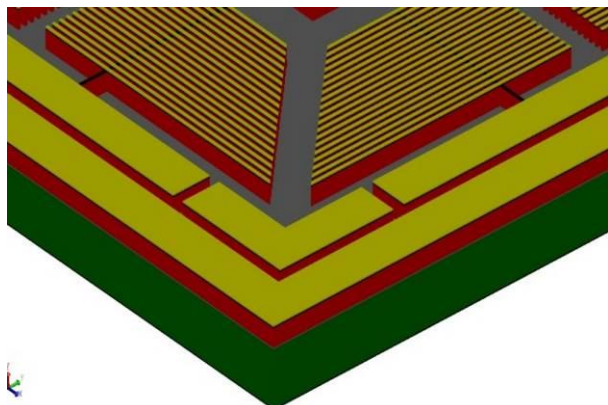


	Silicon Oxide		SOI device layer		PR
	BOX			SOI handle layer	

(4) Trench1 DRIE

The exposed regions of the device layer are etched all the way to the buried oxide layer. The Box layer acts as etch stop.

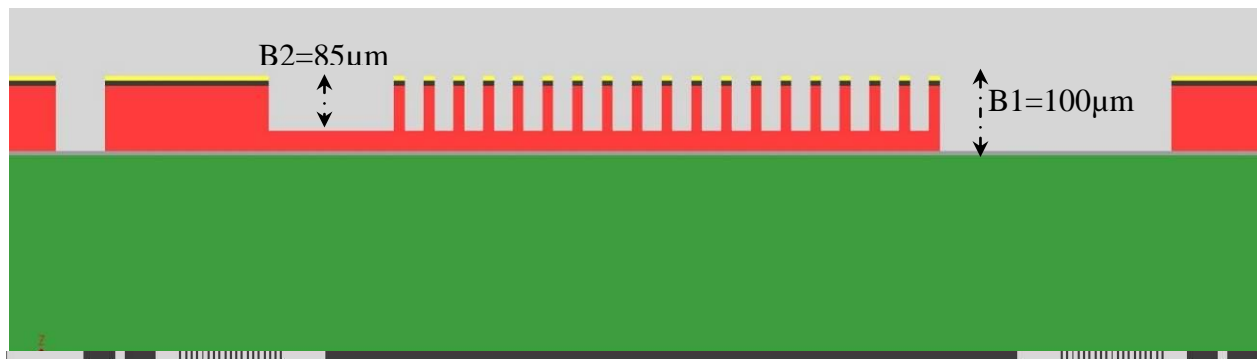
No Mask

Cross-sectional View**CoventorWare 3-D model (left) and microscopic image (right)**

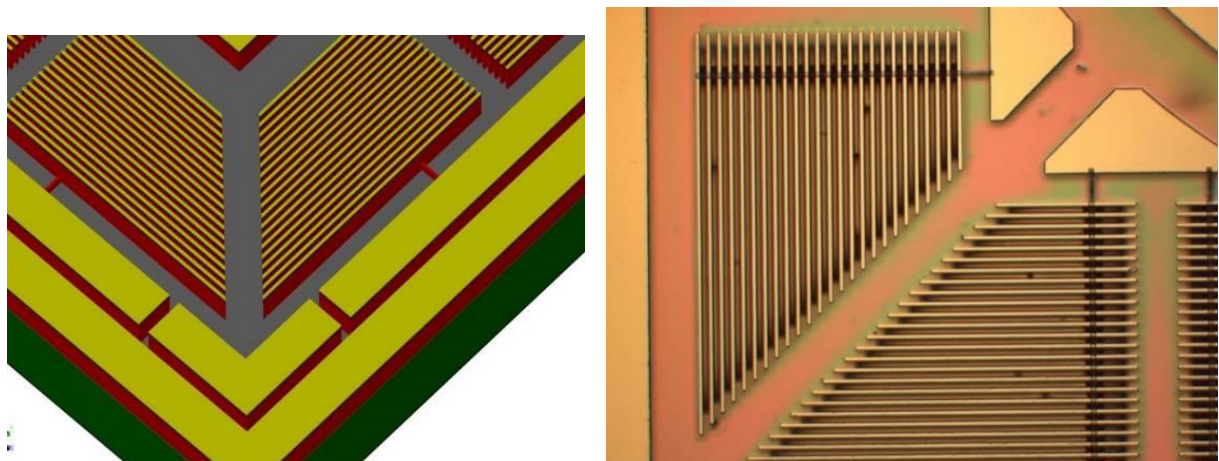
(5) Trench2 DRIE

Silicon Oxide regions which are not covered by the second mask (PR) are etched using (RIE), followed by timed DRIE etching of the exposed regions of device layer to a depth of 85 μm . In other words, only the regions that are covered by the two masks will not be etched.

Cross-sectional View

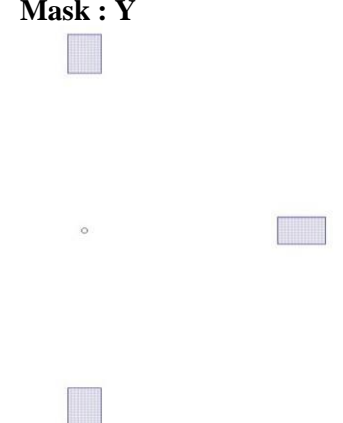
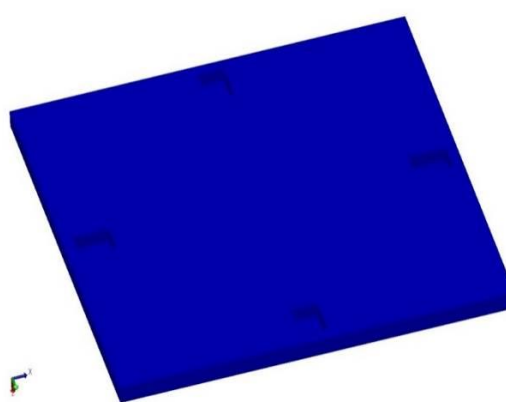
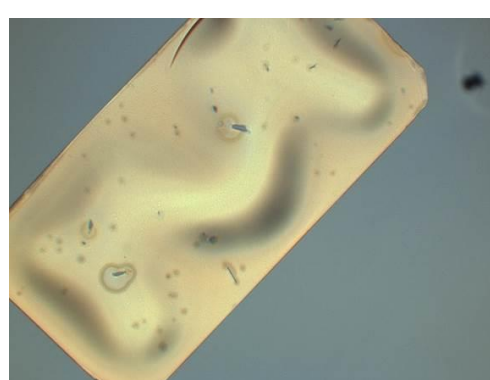


CoventorWare 3-D model (left) and microscopic image (right)



Silicon Oxide	SOI device layer	PR
BOX	SOI handle layer	

4.3.2. Mirror SOI Wafer Fabrication (Upper Structure)

(6) Beam thickness patterning							
A Mirror SOI wafer with device layer thickness of 100 µm is used to form the upper comb fingers. The front side of the silicon wafer is lithographically patterned through (Y) mask. This mask defines the thickness of the suspension springs of the structure, so that in the next steps, these rectangles are etched from the back side to create the suspension springs. The exposed regions of the Y mask is etched using DRIE up to a depth of 85 µm, so that the distance from the bottom of the trenches to the BOX layer equals the height of the springs (h), which is 15 µm. Please refer to the cross-sectional view.	<p style="text-align: center;">Mask : Y</p> 						
Cross-sectional View							
							
CoventorWare 3-D model (left) and microscopic image (right)							
							
<table border="1" style="width: 100%; text-align: center;"> <tr> <td style="width: 25%;">■ Silicon Oxide</td> <td style="width: 25%;">■ SOI device layer</td> <td style="width: 25%;">■ PR</td> </tr> <tr> <td>■ BOX</td> <td>■ SOI handle layer</td> <td></td> </tr> </table>		■ Silicon Oxide	■ SOI device layer	■ PR	■ BOX	■ SOI handle layer	
■ Silicon Oxide	■ SOI device layer	■ PR					
■ BOX	■ SOI handle layer						

(7) Wafer bonding

The Base SOI wafer (upper wafer), which has alignment marks on the bottom side of its handle layer, is bonded with the patterned Mirror wafer using eutectic bonding. The direct bonding did not work with these structures, and that might be due to the roughness of both patterned structures. The eutectic bonding was used as alternative to the direct bonding and it also has an advantage in the following steps of the fabrication process as it acts as an etch stop layer during DRIE of Z mask.

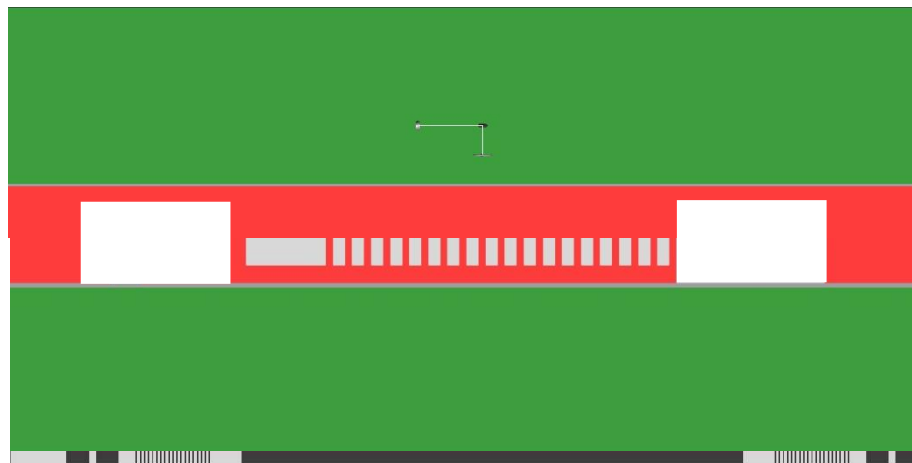
The following are the specifications of the eutectic bonding recipe:

- 1- The eutectic alloy used was Platinum and Gold. A Platinum layer of 200 nm was first deposited on the upper SOI wafer. Then, a 500 nm layer of gold was deposited on the Pt layer.
- 2- The eutectic temperature of the gold is 370 °C. Therefore, the temperature in the recipe was above the eutectic temperature, i.e. 450 °C.
- 3- The applied force on the stack is 1000 N.

Aluminum is another option of eutectic alloy to avoid the high cost of gold, but the drawback of this option is the need for a high temperature of 700 °C to achieve the bonding as the eutectic temperature of Aluminum is 680 °C.

The wafers were aligned prior to bonding using the alignment marks on both wafers. Although the bonding alignment is usually not accurate, as there is a chance of misalignment of 5µm, this misalignment does not affect the alignment of comb fingers because the upper structure fingers would be patterned and aligned after bonding (step 9).

Cross-sectional View



Silicon Oxide	SOI device layer	PR
BOX	SOI handle layer	

(8) Removal of the handle layer of the upper wafer

The handle layer of the upper structure is completely removed using DRIE. But unfortunately a very aggressive DRIE recipe was used, which resulted in the breaking of the thin rectangles that is used to define the thickness of the springs.

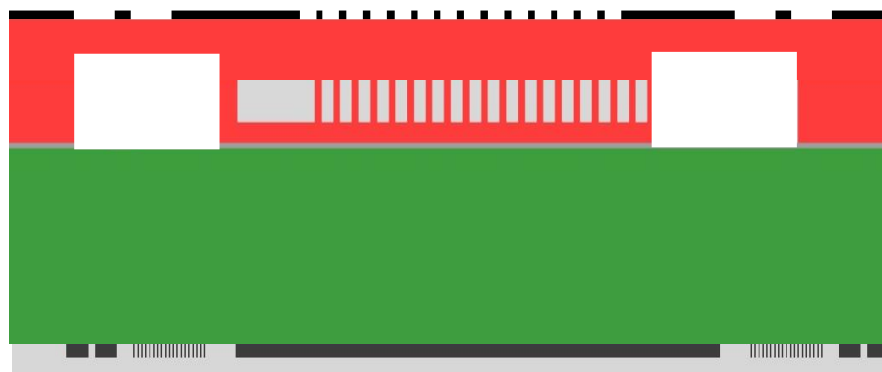
Cross-sectional View



(9) Patterning and etching of the upper BOX layer

The BOX layer is patterned and etched using Mask Z, which defines the features of the upper fingers. The mask is aligned based on the bottom alignment mask using a back side alignment technique, which produces a very precise alignment as it has a tolerance of 0.5 μm.

Cross-sectional view

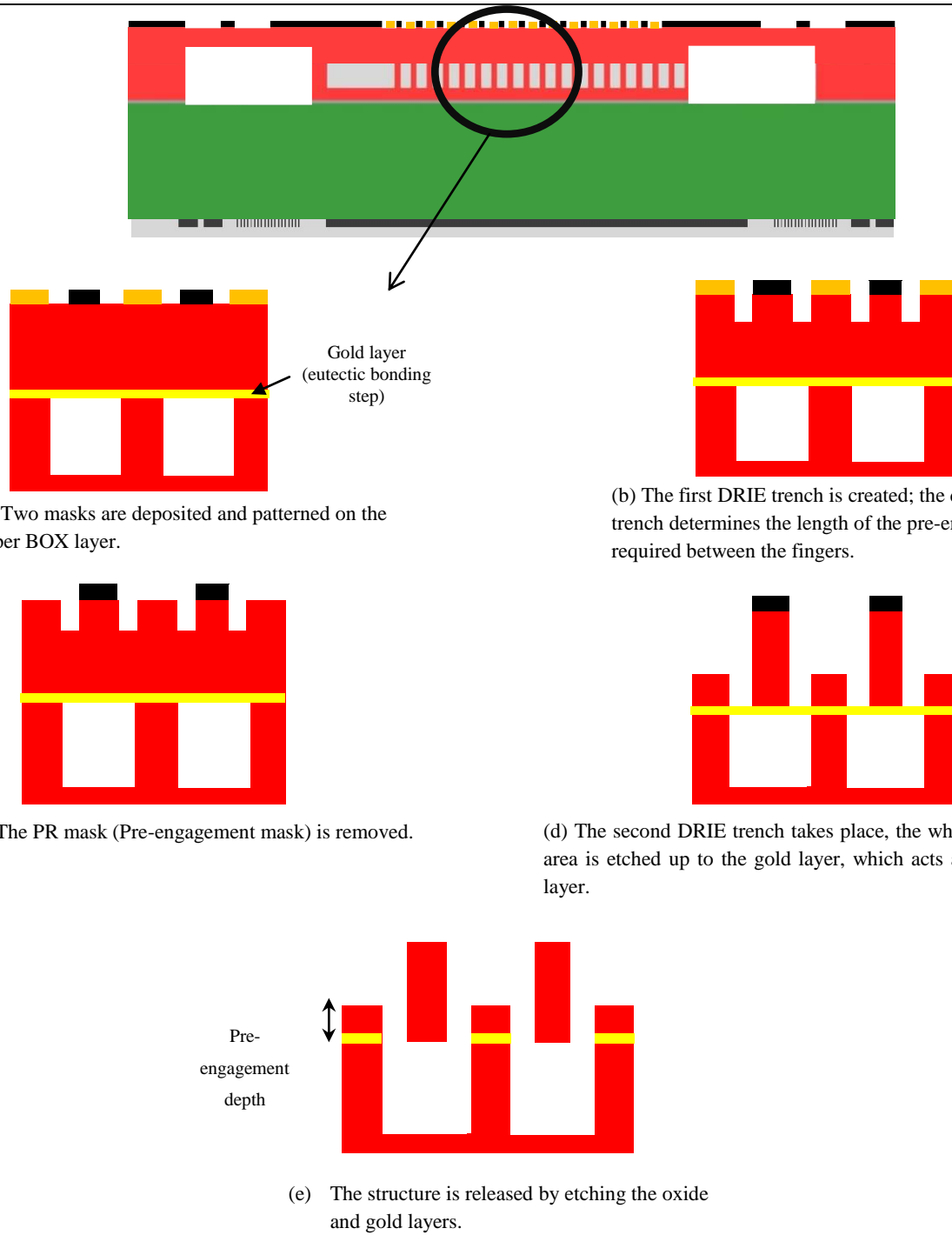


Silicon Oxide	SOI device layer	PR
BOX	SOI handle layer	

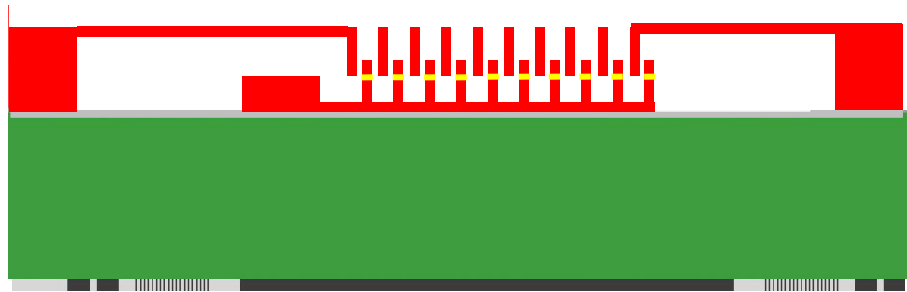
(10) Patterning of the pre-engagement mask and etching the electrodes

Another PR layer is deposited and patterned using pre-engagement mask. The goal of the pre-engagement mask is to create an initial engagement between the upper and the lower fingers. The patterns of the mask face the tips of the lower fingers. This step will be more understood using the schematics below.

Cross-sectional view



The cross sectional-view of the final structure



Chapter 5

Experimental Analysis

In this chapter, an experimental analysis of the 3-DOF MEMS electrostatic vertical comb-drive actuator (VCDA 1) is presented. The analysis includes static and dynamic performances of the actuators during translation and rotation modes. Each mode of motion required a different apparatus to run the tests. The output force test was conducted on VCDA 2 due to its ability to accommodate a mass of 3 mg as the outer rotor diameter is 3 mm as opposed to 1 mm plate diameter in VCDA 1.

5.1. Static and Dynamic Analysis of VCDA 1

5.1.1. Translation Mode Analysis

Static Performance Analysis

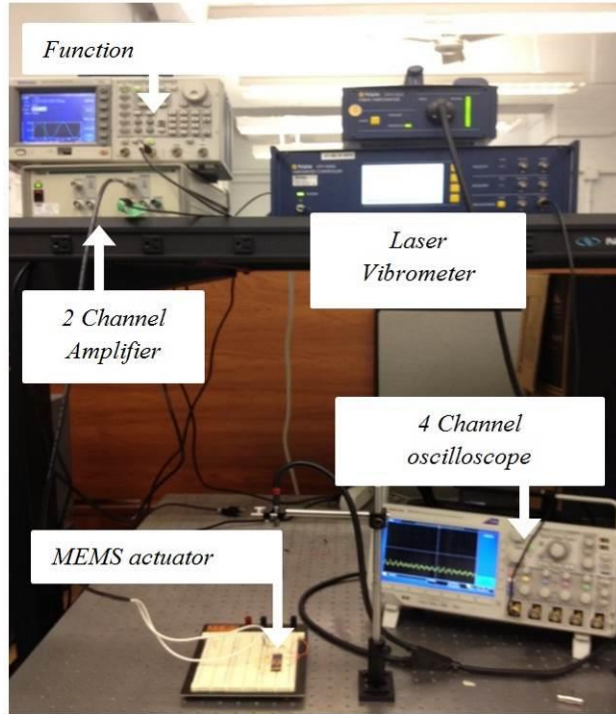


Figure 5-1. Setup used for the static and dynamic performance testing of the actuator in the translation mode.

The apparatus shown in Figure 5-1 was used to assess the static and the dynamic performances of the translational motion of VCDA 1 under different values of the input voltage. The

experimental setup consists of a laser vibrometer, a function generator, a 2-channel amplifier, and an oscilloscope. The vibrometer was used to measure the translational stroke of the actuator by using a laser beam of sub-micron diameter that is oriented to the surface of the plate of the actuator. The vibrometer receives and analyzes the reflected beam, and it reads the vertical motion of the actuator as a voltage signal with a user pre-specified resolution in the ($\mu\text{m}/\text{V}$) range. The output voltage signal of the vibrometer is then displayed on the oscilloscope.

Different values of the DC input voltage were induced across the rotor and stators of the actuator, and the actual linear vertical displacements versus the input voltages were recorded and plotted in Figure 5-2. A maximum translational stroke of 28 μm was achieved at an input voltage of 80 V. The stroke was limited to 28 μm due to the height of the upper electrodes in the Mirror device layer which was only 30 μm , specified by the dimension rules of the first trial run of the MASP fabrication process. A larger stroke could be achieved if the height of the Mirror device layer was larger. To the best knowledge of the author, this is the highest pure translation stroke ever achieved by an electrostatic vertical comb-drive actuator in which there is no magnification mechanism used to enlarge the stroke. There are vertical comb-drive actuators that have achieved more than 28 μm but the initial motion of the actuator is rotational, and magnification mechanism are utilized such as cantilever beams to generate the vertical stroke (e.g. actuators in [39]). In these types of vertical comb-drive actuators, the output force of the actuator significantly decreases due to the magnification process.

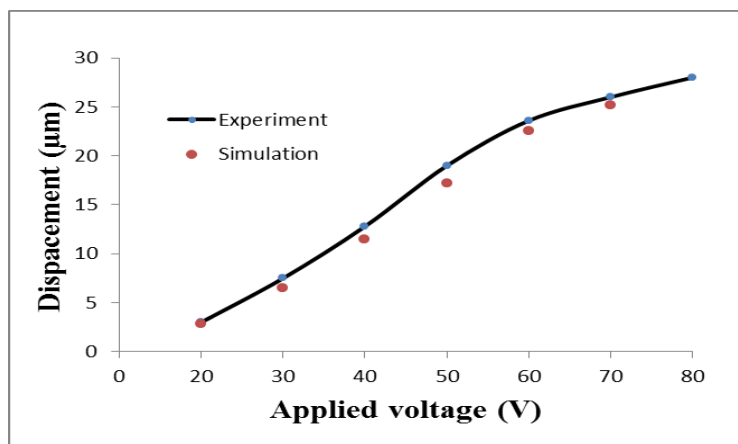


Figure 5-2. Displacement versus voltage of VCDA 1 in the translation mode.

Dynamic Performance Analysis

The dynamic response of VCDA 1 was investigated in the time and frequency domains. First, a dynamic performance test was conducted in the time-domain by applying a step input voltage across the rotor and all of the three stators, so that the actuator plate moves in the vertical direction in a pure translation. The second test was conducted in order to assess the performance at various frequencies by applying a voltage sinusoidal sweep function across the rotor and the stators. The testing apparatus for the static performance analysis was also used for the dynamic analysis (see Figure 5-1).

Figure 5-3 shows the dynamic response of the actuator in the time domain when a unit step input of 0 V to 40 V (the actuator plate is vertically moving down towards the substrate), and 40 V to 0V (the actuator plate is moving up to the equilibrium position) was applied to the system.

A plot of the measured response indicates the absence of any overshoot in the system, which is attributed to the squeeze film damping in the system between the actuator plate and the substrate. The measured settling times of the actuator during the downward stroke (voltage rises) and upward stroke (voltage drops) were about 8 ms and 4 ms, respectively. The slow response of the downward stroke is also attributed to the squeeze film effects in the system.

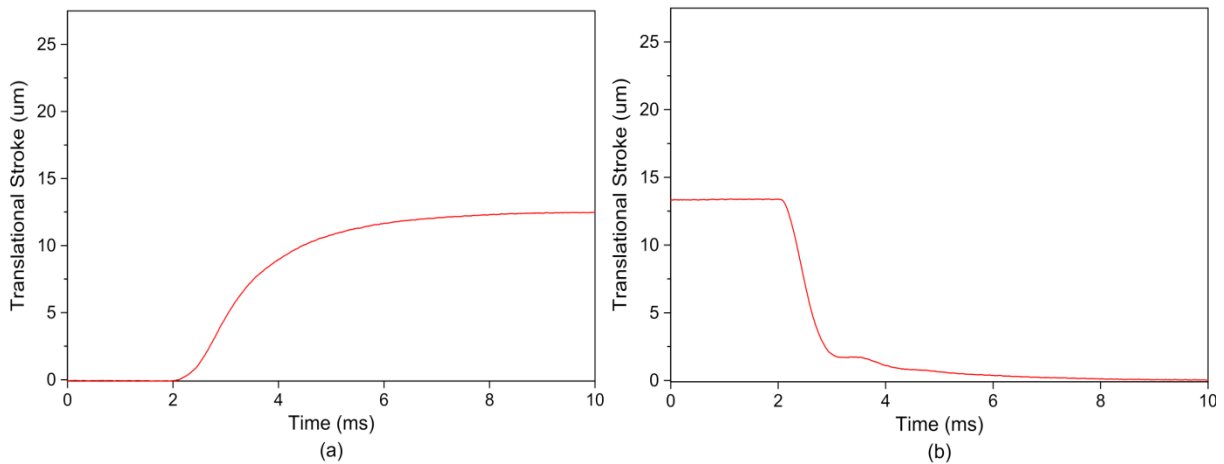


Figure 5-3. Dynamic performance of VCDA 1 in the time domain. (a) Step input of 0 to 40V. (b) Step input of 40 V to 0 V.

For the frequency analysis, a sweep voltage function consisting of a combination of a DC voltage and an AC sinusoidal voltage signal was applied to the system. The frequencies of the sweep

function ranged from 1 Hz to 2000 Hz. Figure 5-4 shows the frequency response of the system. It was observed that no resonance took place in the system response due the large value of the damping ratio (ξ). The measured bandwidth was 160 Hz at -3 dB cut-off line. By investigating the measured frequency response of the system, there are two poles in the system: one starts at 90 Hz with a -20 dB slope of the magnitude curve, whereas the second pole starts at 820 Hz with -40 dB slope of the magnitude curve. The latter indicates a natural frequency of the actuator which lies within the range of the simulated natural frequency (960 Hz).

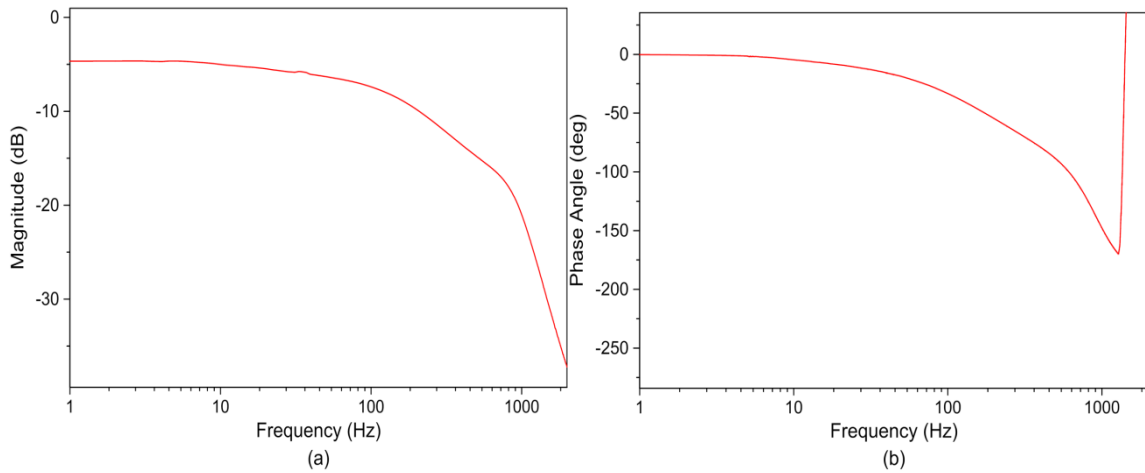


Figure 5-4. Dynamic performance of the translation stroke of VCDA 1 in the frequency domain. (a) Magnitude response. (b) Phase response.

5.1.2. Rotation Mode Analysis

The static and dynamic performances of VCDA 1 in the rotation mode were assessed using the testing apparatus shown in Figure 5-5. The apparatus consists of a position sensing diode (PSD), a waveform generator, a laser source, and an oscilloscope. The PSD is used to measure the rotational stroke of the actuator plate about the x and y axes by detecting the position of the reflected laser spot in the x - y plane. Hence, the angle of rotation of the actuator plate is calculated using triangulation. In order to have accurate measurements, the laser beam reflected by the actuator plate must be orthogonal to the surface of the PSD. The resolution of the PSD was 1 mm/1V.

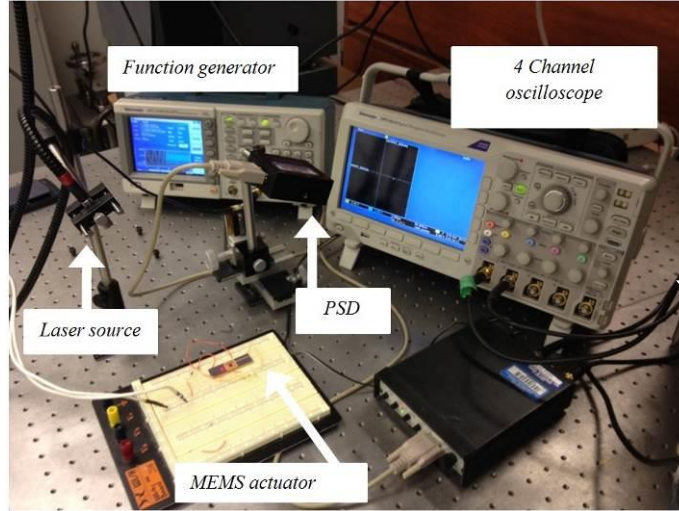


Figure 5-5. Setup used for the static and dynamic performance testing of the actuator in the rotation mode.

Static Performance Analysis

The measurement method started by directing the collimated laser beam to one edge of the actuator plate, and this beam was reflected to the surface of the PSD. At the equilibrium state, when all three stators are zero ($V_1 = V_2 = V_3 = 0$), the PSD reading was zero for both the x and y axes. When a DC input voltage was applied to stators 1 and 2 ($V_1 = V_2 = 50$ V, $V_3 = 0$), the actuator plate was tilted and the PSD readings showed a rotation angle of 0.54°. Figure 5-6 shows the measured rotation angles of the actuator plate at different values of the input voltage; a maximum rotation angle of 0.78° was achieved at an input voltage of 70V ($V_1 = V_2 = 70$ V, $V_3 = 0$).

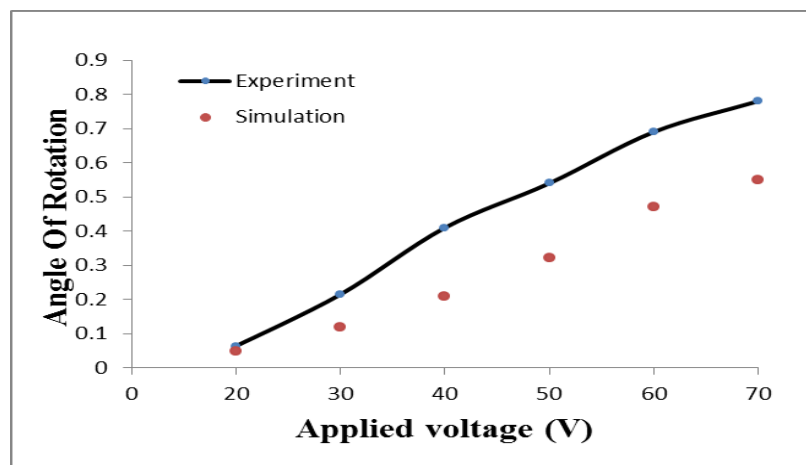


Figure 5-6. Angle of rotation versus applied voltage of VCDA 1 in the rotation mode.

Dynamic Performance Analysis

The dynamic analysis of VCDA 1 in the rotation mode was conducted in the time domain. The testing apparatus shown in Figure 5-5 was also used for this task. For the time domain analysis, a step input voltage of 0 V to 40 V was applied to stators 1 and 2 while stator 3 remained at zero ($V1=V2=40$ V, $V3=0$). The actuator's unit step response during the actuation is shown in Figure 5-7(a). In order to investigate the rotational stroke when the actuator plate returns to its equilibrium position, all stators were grounded ($V1=V2=V3=0$) and the response is shown in Figure 5-7(b). The plots of the unit step response suggests that the settling times during actuation and release states are about 4 ms and 3 ms. It was observed that the settling times of the rotational stroke is by far less than the settling times for the translational stroke. This is attributed to slide film damping during rotation as opposed to squeeze film damping during translation, where squeeze film damping usually has more impact on the response of the system than slide film damping. Overshoot was noticed during the release state, which might be attributed to the low amount of slide film damping during release in comparison with the actuation state.

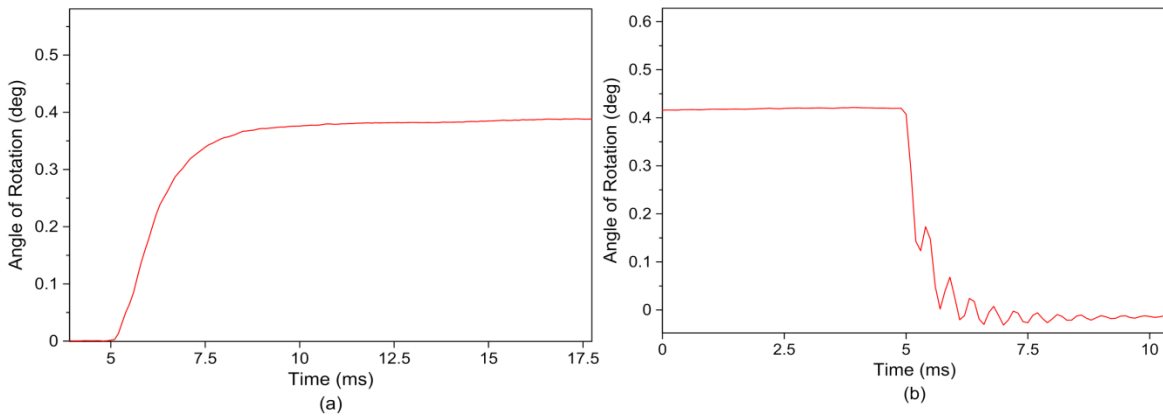


Figure 5-7. Time domain response of VCDA 1 in the rotation mode. (a) Step of 0 to 40V. (b) Step input of 40 V to 0 V.

5.2. Output Force Analysis

The output force test was conducted on VCDA 2 because it has a wider rotor than that of VCDA 1. Different techniques were used to attach the mass load to the actuator plate such as gluing the mass to the actuator plate, putting a drop of carbon paint that solidifies on the plate. But none of them was successful because of the sensitivity of the miniaturized structure to the glue, as the

glue could disperse between the electrodes of the actuator and eventually leads to damaging the chip. The technique eventually used in the experiment for loading the actuator, was to pick up and place the load on the actuator plate using tweezers and then repositioning it at the center of the plate by using a needle. VCDA 2 with a 3 mg mass attached to its rotor is shown Figure 5-8. It was observed that by using this technique, no damage occurred in the actuator and the mass did not slide when an AC voltage was applied; this might be due to the surface attraction force between the mass of the plastic and the surface of the silicon layer of the actuator.

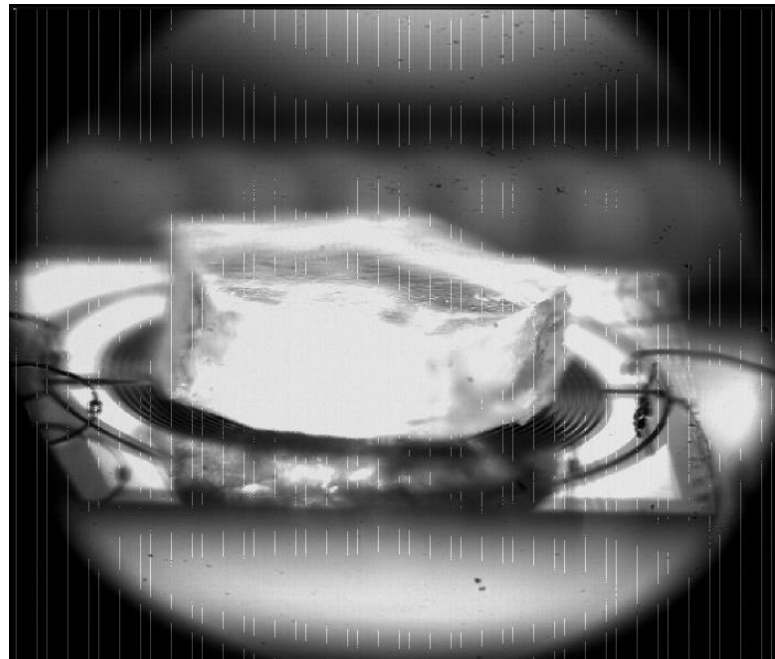


Figure 5-8. Snapshot of VCDA 2 loaded with a mass of 3 mg during the testing.

5.2.1. Static Performance of VCDA 2

Static performance analysis of the un-loaded VCDA 2 was conducted first to compare it with the loaded case. Different values of the DC input voltage were applied to the outer rotor and the outer stators of VCDA 2, and the measured static performance results are plotted in Figure 5-9. A mass of 3 mg of plastic was then attached to the outer rotor of the actuator. The measured static performance results are also shown in Figure 5-9. It was observed that the translation stroke of the loaded actuator was not significantly affected by attaching the load. This is because the outer rotor is very stiff with a numerically estimated natural frequency of 1450 Hz.

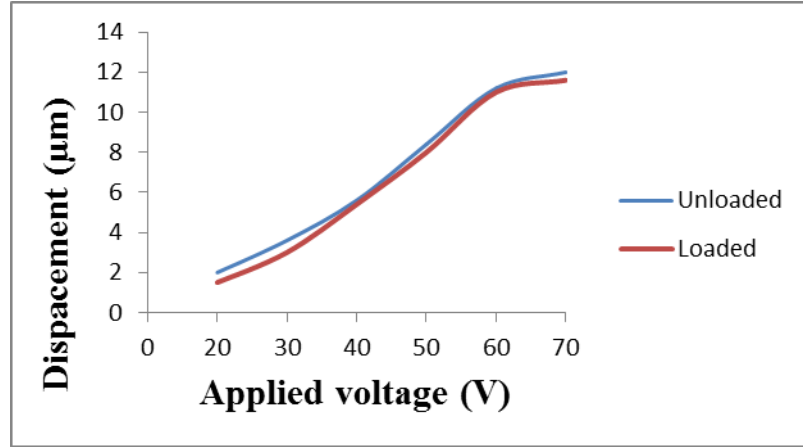


Figure 5-9. Static performance of the translational stroke of the outer rotor of VCDA 2 in the unloaded and loaded states.

5.2.2. Dynamic Performance of VCDA 2

The dynamic response of VCDA 2 was also conducted for the unloaded and loaded states in the time domain. The step input response during the actuation and the release of the outer rotor for both states are shown in Figure 5-10 and

Figure 5-11, respectively. By investigating the plots, the measured settling times of the unloaded and loaded cases when the voltage raises were 5 ms and 10 ms, respectively, and when the voltage drops, the settling times were 3 ms and 12 ms, respectively. Overshoot was observed in the loaded case which might be due to the fact that the load was not perfectly attached to the load.

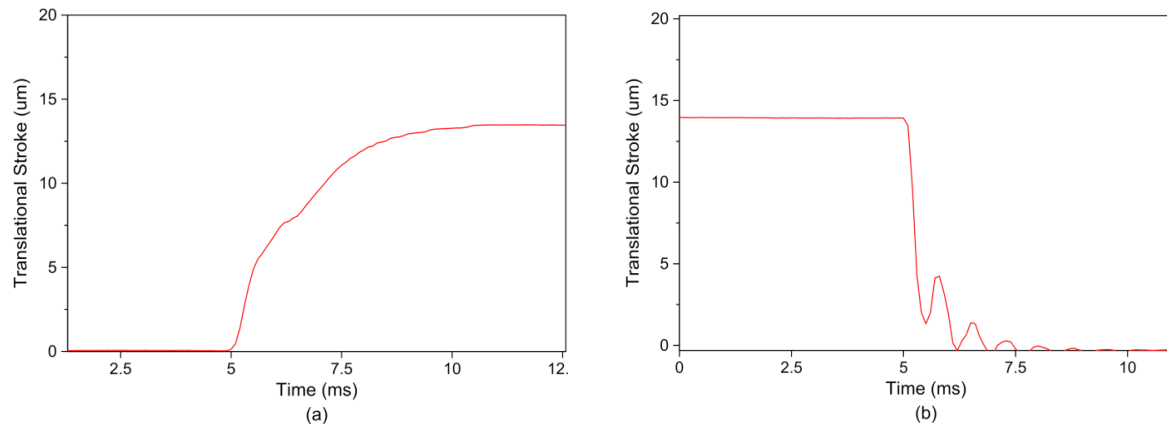


Figure 5-10. Dynamic performance of the unloaded outer rotor of VCDA 2 in the time domain. (a) Step input of 0 to 80 V. (b) Step input of 80 V to 0 V.

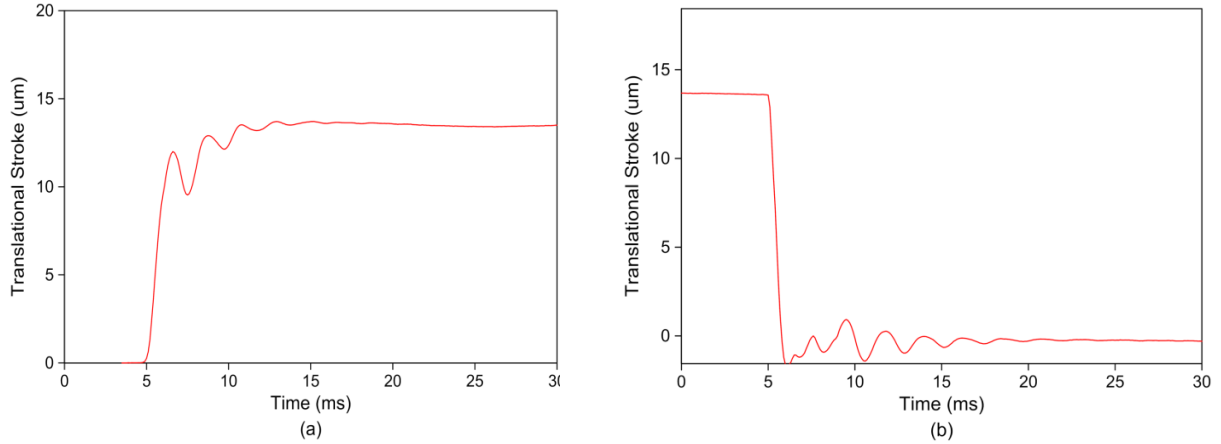


Figure 5-11. Dynamic performance of the 3 mg loaded outer rotor of VCDA 2 in the time domain. (a) Step input of 0 to 80V. (b) Step input of 80 V to 0 V.

5.3. Experimental Results Summary

As a summary, VCDA 1, which was optimized in terms of out-of-plane stroke, achieved a translation stroke of 28 μm at an input voltage of 80 V, and an angle of rotation of 0.78 $^{\circ}$ at 70 V. The measured natural frequency of the actuator in the translation mode is 820 Hz and the measured bandwidth is 160 Hz.

VCDA 2, which was optimized in terms output force, was able to vertically displace a mass load of 3 mg for 13.5 μm at 80 V. The settling time of the rotor during the actuation state (step input voltage from 0 V to 80 V) and release (step input voltage from 80 V to 0 V) were measured as 10 ms and 12 ms, respectively.

Chapter 6

Conclusions and Contributions

6.1. Conclusions

A novel MEMS electrostatic vertical comb-drive actuator that can provide three-degrees-of-freedom motion, translation along the z -axis and rotation about the x and y axes, was developed, fabricated, and tested. The novel actuator provides a high output force as it is attached directly to the load and no mechanical amplification mechanisms are used.. The novel actuator overcomes the limitations of conventional comb-drive actuators such as fingers misalignment, and lateral instability by using a new fabrication process and a novel flexure mechanism. The flexure mechanism utilizes high in-plane stiffness of the vertical comb-drive actuator compared to the z -axis stiffness of the actuator.

Two versions of the actuator were developed and fabricated using the MASP fabrication process. The accuracy of this process reduced the misalignment issue that is usually associated with the fabrication of conventional VCDA. The measured misalignment between the comb electrodes was about 0.005%. The first version (VCDA 2) was able to achieve a maximum translation (piston) stroke of 28 μm at 80 V. The measured undamped natural frequency of the actuator was 820 Hz; however, it has a limited measured bandwidth of 160 Hz, which is attributed to the presence of non-negligible squeeze film effects in the system. The settling times of the actuator during the actuation and the release were about 4 ms and 3 ms, respectively. In the rotation mode, the actuator was able to achieve an angle of rotation of 0.78° at 70 V.

The second version (VCDA 2) has a large outer rotor which was utilized to perform the output force analysis of the novel actuator. The actuator was tested and characterized in both the unloaded and loaded states. The outer rotor of the actuator was able to achieve a translational stoke of 13.5 μm at 80 V. The measured settling times of the loaded and unloaded cases (voltage raises) were 5 ms and 10 ms, respectively, whereas the settling time when the voltage drops were 3 ms and 12 ms, respectively.

An improved version of the novel 3-DOF MEMS actuator was developed to be used for auto-focus in phone cameras. The actuator utilizes only one degree of freedom of the 3-DOF MEMS electrostatic VCDA, i.e. translation stroke along the z -axis. It was developed, simulated and

analyzed using CoventorWare. The actuator was able to move a lens of 3 mg for 78 μm at 70 V, and it has an undamped natural frequency of 430 Hz. Another version of the novel actuator was also developed to achieve image stabilization in phone cameras, which only utilizes two degrees of freedom of the 3-DOF MEMS electrostatic actuator, which are rotations about the x and y axes. The simulation analysis showed that the actuator was able to rotate a mass of 560 mg for a rotation angle of 0.6°, and it has a frequency bandwidth of 110 Hz, which meets the requirements of the OIS feature in cell phone cameras.

The fabrication of the AF and OIS actuators was attempted by using a modified version of the MASP fabrication process; however, about 8 fabrication steps out of 12 were successfully achieved; however, the final four steps were left for future work.

6.2. Contributions

The significant contributions of this work are:

1. Development of a novel flexure mechanism for MEMS electrostatic vertical comb-drive actuator that improved the vertical stroke
2. Development of a novel 3 degrees-of-freedom MEMS electrostatic vertical comb-drive actuator
3. Development of a high output force MEMS electrostatic vertical comb-drive actuator
4. Design of a MEMS electrostatic actuator that satisfies the requirements of the AF functions in cell phone camera by vertically displacing a lens of 3 mg for 78 μm while offering a high speed response of <10 ms
5. Design of a MEMS electrostatic actuator that satisfies the requirements of the OIS feature in cell phone cameras by rotating the complete camera module by an angle of 0.6° to eliminate yaw and pitch rotations of the hand

6.3. Recommendations

It is recommended that the 3-DOF MEMS electrostatic VCDA be further explored and enhanced. First, the stroke of the actuator can be further improved by optimizing the dimensions of the

supporting beams of the actuator, so that the actuator rotor is much stiffer along the x - y plane, compared to the z -axis stiffness. That includes exploring different types of beams such as guided cantilever beams, serpentine beams, and folded flexure.

Second, the rotation angle of the actuator can be further enhanced by increasing the gap between the fingers of the comb-drive actuator. That, though, would compromise the low voltage advantage of the comb-drive actuator. However, this can be utilized in micromirror applications in which using a high voltage is not an issue.

Third, the operating voltage could be further decreased in order to use the actuator for AF in cell phone cameras by decreasing the gap between the fingers of the upper and lower combs. Although decreasing the gap between the fingers would limit the angle of rotation of the actuator, the AF actuator utilizes only the translation mode of the actuator. Therefore, by decreasing the gap, the electrostatic force would dramatically increase, which in turn will eliminate the need for high operating voltage.

Fourth, the modified version of the Micralyne All-Silicon Platform fabrication process should be further pursued to fabricate the AF and OIS actuators with the required features.

References

- [1] DigitalOptics Corporation, “Smartphone Camera Advances Made Possible by MEMS-cam Technologies,” white paper, Feb. 2013.
- [2] R. C. Gutierrez, E. R. Fossum, and T. K. Tang, “Auto-Focus Technology,” in *the 2007 International Image Sensor Workshop*, 2007.
- [3] C. S. Liu, P. D. Lin, P. H. Lin, S. S. Ke, Y. H. Chang, and J. Bin Horng, “Design and Characterization of Miniature Auto-Focusing Voice Coil Motor Actuator for Cell Phone Camera Applications,” *IEEE Trans. Magn.*, vol. 45, no. 1, pp. 155–159, Jan. 2009.
- [4] H. Ren and S. Wu, “Variable-focus Liquid Lens,” *Opt. Soc. Am.*, vol. 15, no. 10, pp. 5931–5936, 2007.
- [5] H. P. Ko, H. Jeong, and B. Koc, “Piezoelectric Actuator for Mobile Auto Focus Camera Applications,” *J. Electroceramics*, vol. 23, no. 2–4, pp. 530–535, Jun. 2008.
- [6] D. J. Jayaraj, “MEMS: Next Generation Auto-Focus for HD Video,” *Tessera Technology Symposium*, 2010. [Online]. Available: http://www.tessera.com/abouttessera/upcomingevents/Documents/4_MEMS_Korea2010.pdf.
- [7] L. K. Lai and T. S. Liu, “Design of Auto-Focusing Modules in Cell Phone Cameras,” *Int. J. Smart Sens. Intell. Syst.*, vol. 4, no. 4, pp. 568–582, 2011.
- [8] G. W. Roman C. Gutierrez, “Lens Barrel with MEMS Actuator,” US 2012121242A12012, May 2013.
- [9] E. Or and D. Pundik, “Hand Motion and Image Stabilization in Hand-held Devices,” *IEEE Trans. Consum. Electron.*, vol. 53, no. 4, pp. 1508–1512, Nov. 2007.
- [10] R. Safaei-Rad and M. Aleksic, “Handshake Characterization and Image Stabilization for Cell-Phone Cameras,” *SPIE-IS&T*, vol. 7241, pp. 72410V1–72410V15, Jan. 2009.

- [11] B. Golik and D. Wueller, "Measurement Method for Image Stabilizing Systems," *SPIE-IS&T Electron. Imaging*, vol. 6502, pp. 65020O1–65020O10, 2007.
- [12] A. Benjamin and D. Brown, "Camera Apparatus Having an SMA Actuator System," US 8,570,384 B22013, Oct. 2013.
- [13] "Image Stabilization." [Online]. Available: http://en.wikipedia.org/wiki/Image_stabilization.
- [14] M. Eromäki, "Optical image stabilization," WO 2013076350 A1, May 2013.
- [15] HTC, "Optical Image Stabilization in HTC one," 2013. [Online]. Available: <http://www.htc.com/www/zoe/stabilization/>.
- [16] E. Simon, B. Berge, H. Gaton, O. Jacques-sermet, F. Laune, J. Legrand, M. Maillard, N. Moine, and N. Verplanck, "Optical Image Stabilization with a liquid lens," *Opt. Soc. Am.*, 2010.
- [17] L. Xiaolei, R. C. Gutierrez, P. K. Leang, J. A. Mendez,, C. Zaharia, and A. F. Drimbarean, "Mems-Based Optical Image Stabilization," US 2013/0077945 A1, Mar. 2013.
- [18] D. Sachs, S. Nasiri, and D. Goehl, "Image Stabilization Technology Overview.", white paper, InvenSense Inc.
- [19] C. Liu, "Electrostatic Actuation," in *Foundations of MEMS*, Second., 2005, pp. 127–168.
- [20] "Piezoelectricity," *Wikipedia*. [Online]. Available: <http://en.wikipedia.org/wiki/Piezoelectricity>.
- [21] T. J. Lewis, "Fundamentals of the Electret State and the Interfacial Origin of Piezoelectricity," *Proc. 8th Int. Symp. Electrets (ISE 8)*, 1994.
- [22] A. Ballato, "Piezoelectricity: history and new thrusts," *1996 IEEE Ultrason. Symp. Proc.*, vol. 1, 1996.
- [23] D. Thorstein Wang, K. H. Haugholt, T. Frode, W. E. Booij, and I.-R. Johansen, "Polymer Lens," US 8,199,410 B22012, Jun. 2012.

- [24] E. Simon, B. Berge, F. Fillit, H. Gaton, M. Guillet, O. Jacques-sermet, F. Laune, J. Legrand, M. Maillard, and N. Tallaron, “Optical Design Rules of a Camera Module with a Liquid Lens and Principle of Command for AF and OIS functions.” *Proc. SPIE*, Vol. 7849, 2012.
- [25] R. Waldingbrett, “ELECTROSTATIC COMB-DRIVE ACTUATOR DESIGN,” tech. report, *Vestfold University College*, 2009.
- [26] H. Toshiyoshi, “Electrostatic Actuation,” in *Comprehensive Microsystems*, 2008, pp. 1–38.
- [27] R. Kalyanaraman, M. Packirisamy, and R. Bhat, “Nonlinear Pull-In Study of Electrostatically,” *IEEE*, pp. 195–199, 2005.
- [28] B. Borovic, F. L. Lewis, A. Q. Liu, E. S. Kolesar, and D. Popa, “The Lateral Instability Problem in Electrostatic Comb-drive Actuators: Modeling and Feedback Control,” *J. Micromechanics Microengineering*, vol. 16, no. 7, pp. 1233–1241, Jul. 2006.
- [29] I. P. M. Wickramasinghe and J. M. Berg, “Lateral Stability of a Periodically Forced Electrostatic Comb Drive,” *2012 Am. Control Conf.*, pp. 80–85, 2012.
- [30] E. T. Carlen, S. Bakshi, a. Pareek, and C. H. Mastrangelo, “High-aspect ratio vertical comb-drive actuator with small self-aligned finger gaps,” *J. Microelectromechanical Syst.*, vol. 14, no. 5, pp. 1144–1155, Oct. 2005.
- [31] K. Oda, H. Takao, K. Terao, T. Suzuki, F. Shimokawa, I. Ishimaru, and F. Oohira, “Vertical Comb-drive MEMS Mirror with Sensing Function for Phase-shift Device,” *Sensors Actuators A Phys.*, vol. 181, pp. 61–69, Jul. 2012.
- [32] V. Milanovic, G. a. Matus, and D. T. McCormick, “Gimbal-Less Monolithic Silicon Actuators for Tip–Tilt–Piston Micromirror Applications,” *IEEE J. Sel. Top. Quantum Electron.*, vol. 10, no. 3, pp. 462–471, May 2004.
- [33] S. He, R. Ben Mrad, and J. Chong, “Repulsive-force Out-of-plane Large Stroke Translation Micro Electrostatic Actuator,” *J. Micromechanics Microengineering*, vol. 21, no. 7, p. 075002, Jul. 2011.

- [34] J. K. Rodney Clark, Jay Hammer, "Vertical Comb drive Actuated Deformable Mirror Device and Method," US20020109894 A12002, May 2002.
- [35] E. Carr, S. Olivier, and O. Solgaard, "Large-Stroke Self-Aligned Vertical Comb Drive Actuators for Adaptive Optics Applications," *SPIE*, vol. 6113, p. 61130T–61130T9, Jan. 2006.
- [36] D. Hah, P. R. Patterson, H. D. Nguyen, S. Member, H. Toshiyoshi, and M. C. Wu, "Theory and Experiments of Angular Vertical Comb-Drive Actuators for Scanning Micromirrors," *IEEE J. Sel. Top. Quantum Electron.*, vol. 10, no. 3, pp. 505–513, 2004.
- [37] J. Lee, J. Kim, Y. Ko, D.Kong, K. Lee, and D. Jeon, "Fabrication of Silicon Optical Scanner for Laser Display," *2000 IEEE/LEOS Int. Conf. Opt. MEMS (Cat. No.00EX399)*, 2000.
- [38] D. A. Henderson, "Micro-Scale Smart Actuator Modules for Imaging Systems," in *ACTUATOR 2012*, Jun. 2012.
- [39] V. Milanovic, S. Kwon, and L. P. Lee, "High Aspect Ratio Micromirrors With Large Static Rotation and Piston Actuation," *IEEE Photonics Technol. Lett.*, vol. 16, no. 8, pp. 1891–1893, Aug. 2004.

Appendix A

Mask Layout of VCDA 1

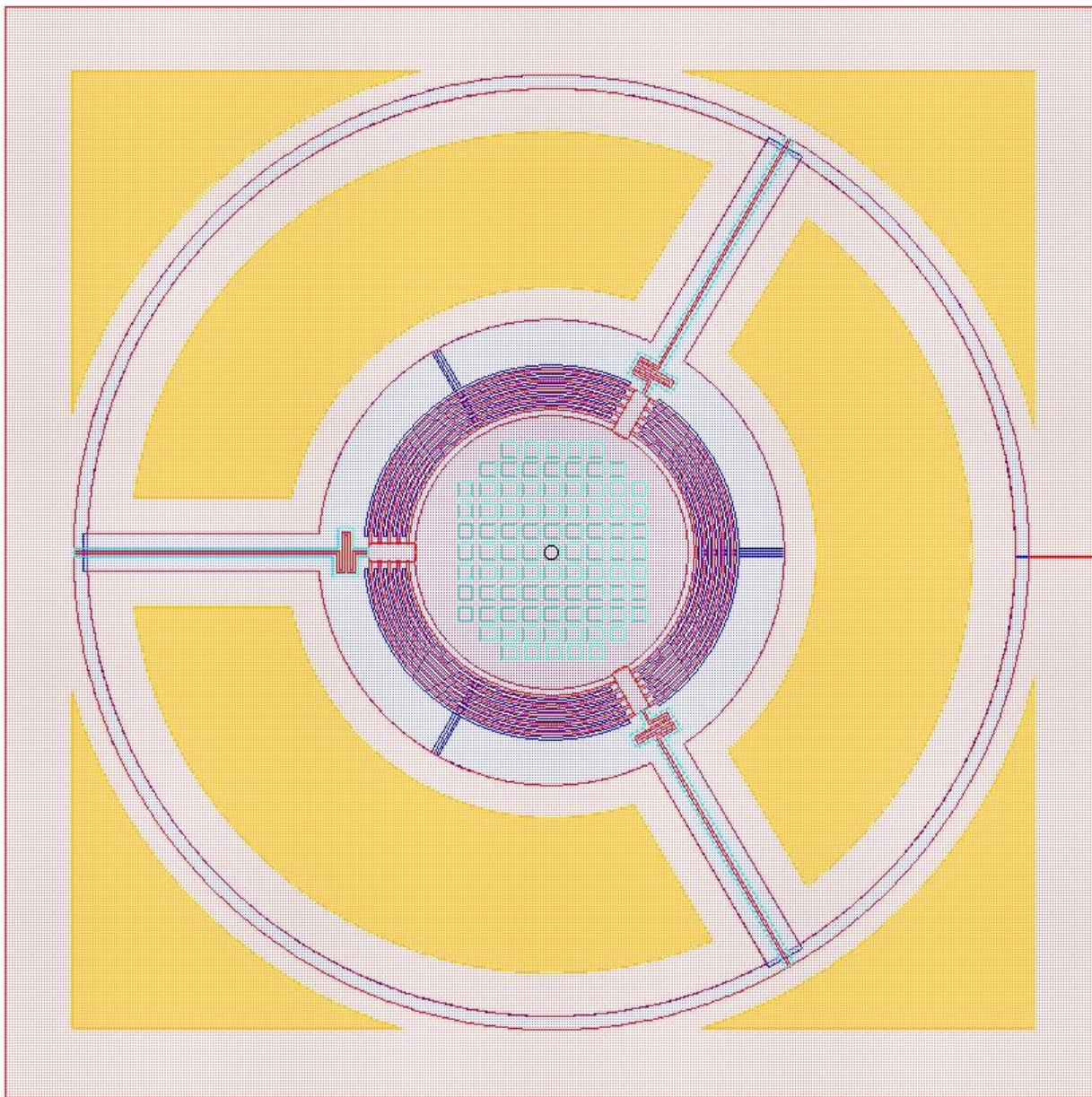


Figure A-1. GDS mask layers forVCDA 1.

Appendix B

Mask Layout of VCDA 2

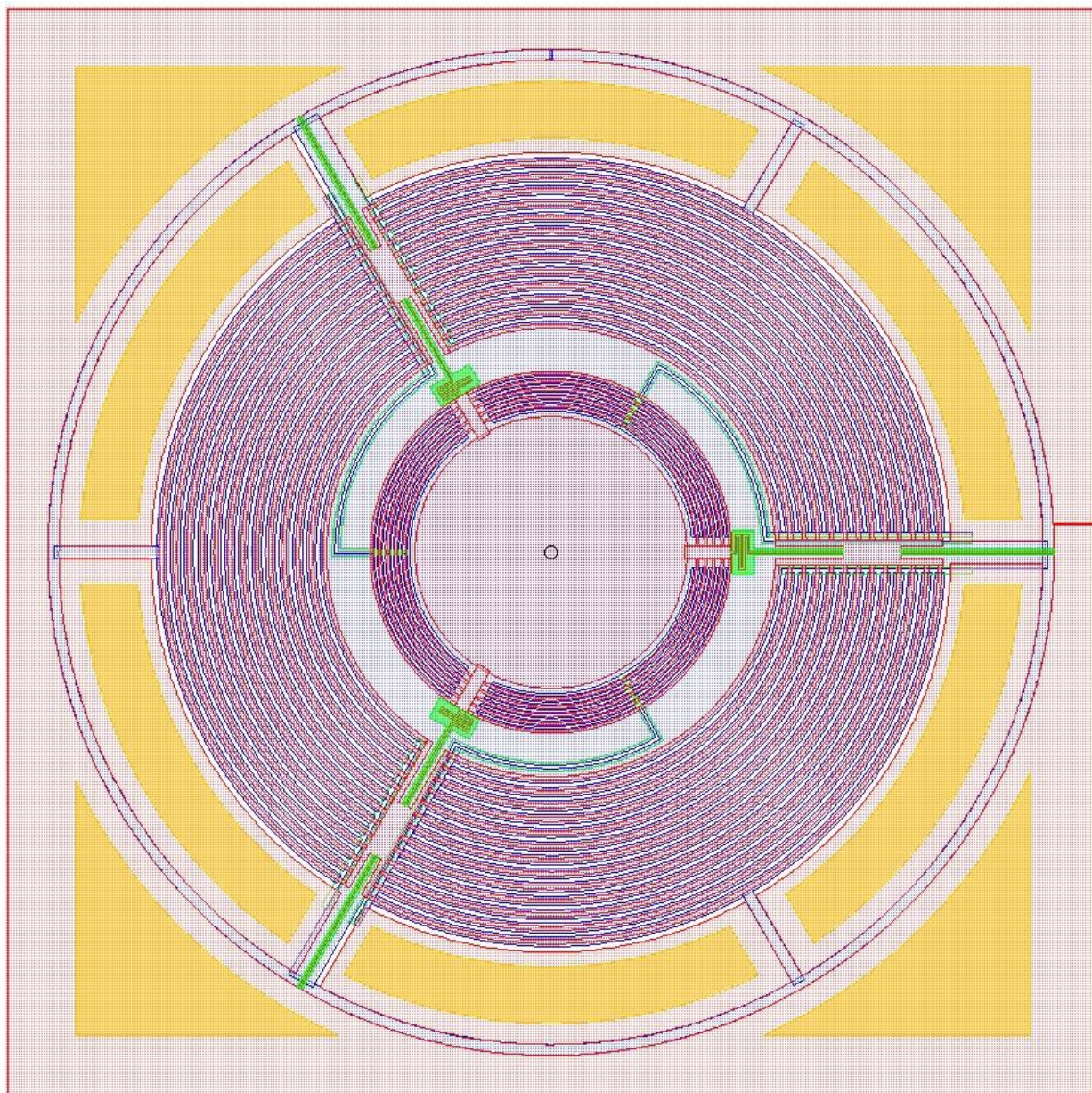


Figure B-1. GDS mask layers for VCDA 2.

Appendix C

Mask Layout of AF Actuator

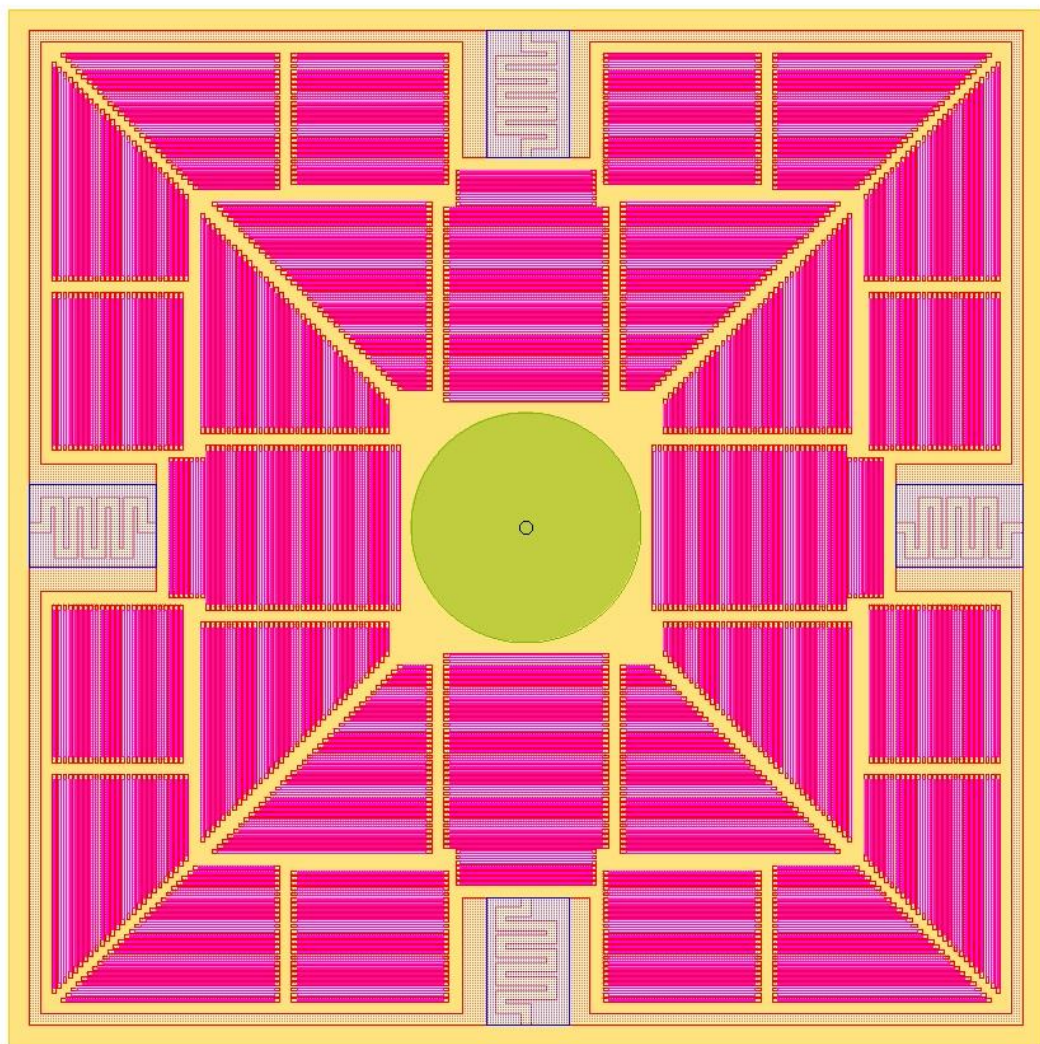


Figure C-1. GDS mask layers for AF actuator.

Appendix D

Mask Layout of OIS Actuator

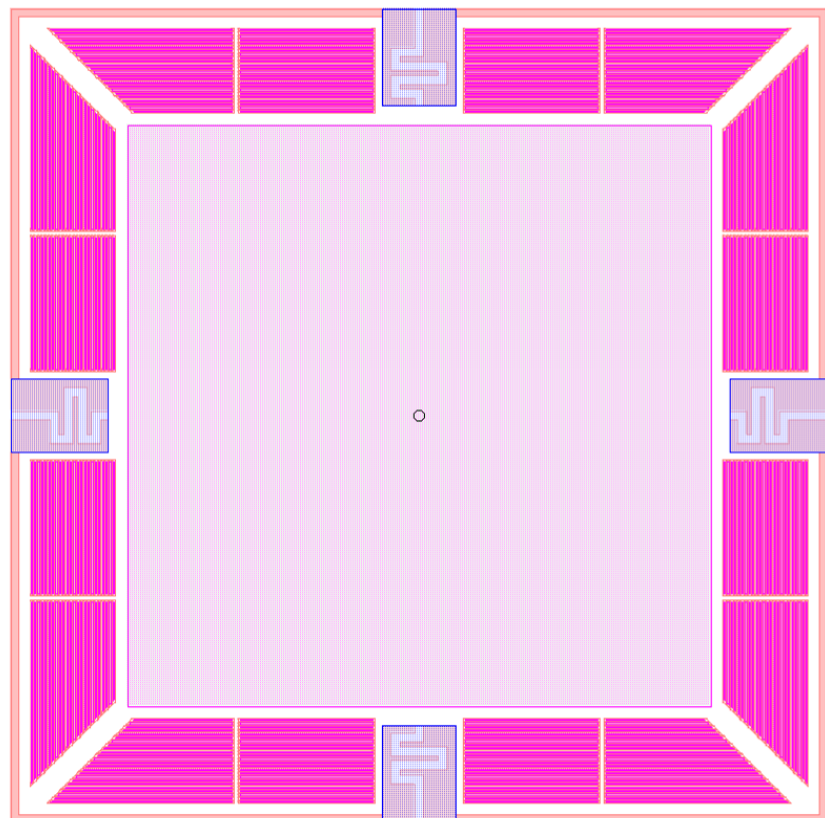


Figure D-1. GDS mask layers for OIS Actuator.